SILICON BASED PHOTONIC CRYSTAL COUPLED TO AN OPTICAL CAVITY FOR HIGHLY SENSITIVE BIODETECTION

BY

TIANTIAN TANG

THESIS

Submitted in partial fulfillment of the requirements
for the degree of Master of Science in Electrical and Computer Engineering
in the Graduate College of the
University of Illinois at Urbana-Champaign, 2015

Urbana, Illinois

Adviser:

Professor Brian T. Cunningham

Abstract

Since its discovery by Sir John Frederick William Herschel in 1845, fluorescence detection technology has developed extensively to be used in disease diagnosis, DNA sequencing, cellular imaging, flow cytometry, forensics, and monitoring processes in biological systems. In order to achieve better sensitivity and higher signal-to-noise ratio (SNR), metal-enhancement fluorescence and nano-engineered surfaces were used to augment the excitation of fluorophores and provide directionality to the emitted light for improved collection. Photonic crystals (PCs), which are composed of periodically refractive index modulated nano-structures, have proven to be a great surface for improving the emission from surface-bound fluorophores. When the resonant guided mode condition is reached, PCs provide fluorescence enhancement mainly through two mechanisms: enhanced excitation and enhanced extraction. This thesis addresses the design, fabrication, and characterization of a silicon based PC coupled to an optical cavity. Compared to an ordinary PC without coupled optical cavity, the new PC can further increase fluorescent output via stronger evanescent field. A fluorescent dye tagged protein detection experiment was conducted on the new PC showing that it provides 10x SNR, opening the door for detection of biomarkers in sub-pg/ml range.

Acknowledgments

First and foremost, I would like to thank my advisor Professor Brian Cunningham for giving me this extraordinary opportunity to learn, grow and work in the Nano Sensors Group (NSG). I can still remember your passionate and vivid description of NSG's bio-sensing technology during our first meeting in my junior year. Without your vision, guidance and kindness, this work would not be possible.

I also want to thank my wonderful team members. Yafang, thank you for being a great big sister to lead me into the project with so much patience. Chenqi and Haisheng, thank you for working hard with me. Lydia and Caitlin, though I only knew you two for less than a year, I really enjoyed our time working and playing together. I will miss your contagious positive attitude!

I am thankful for Hsin-Yu, Gloria, Weili, Jui-Nung and Hoejeong as well. Hsin-Yu, thank you for teaching me while I was a junior who knew nothing about photonic crystals. Gloria, thank you for being an excellent example of an inspiring and strong woman. I will cherish our time spent in snack shops and your encouragement through my tough times. Weili, Jui-Nung and Hojeong, thanks for those deep conversations about technology.

Lastly, I want to thank my parents and friends. Thank you for your generous love and support. Thank you for believing in me. Thank you for everything.

Contents

1. Fluorescence and Methods to Enhance Fluorescence

Fluorescence detection is widely used in life science technology due to its high sensitivity. Since its discovery by Sir John Frederick William Herschel in 1845, fluorescence technology has developed extensively to be used in disease diagnosis, DNA sequencing, cellular imaging, flow cytometry, forensics, and monitoring processes in biological systems. This chapter will discuss the physics behind fluorescence and methods used to enhance fluorescence.

1.1 Fluorescence explained

Fluorescence is a kind of luminescence which typically emanates from aromatic molecules. A Jablonski diagram is often used to describe light absorption and emission. Figure 1 shows a Jablonski diagram in which the singlet ground, first and second states are depicted by S_0, S_1, S_2 respectively. Upon light absorption, a fluorophore is usually excited to higher states - S_1 or S_2. Electrons in S_2 often rapidly relax

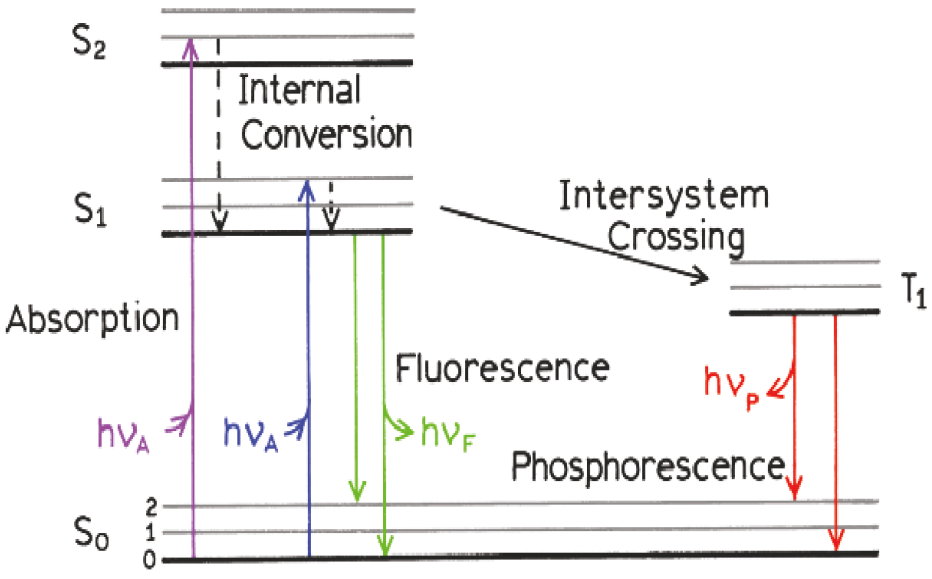

Figure 1 Jablonski diagram for fluorescence [1].

to S_1 within 10^{-12}s to reach thermal equilibrium, then electrons in S_1 will return to ground state S_0.

One can learn from Jablonski diagram that energy of emission is typically less than that of absorption. And this can been seen from the spectra of perylene and quinine sulfate shown in Figure 2. Emission spectra vary widely and are dependent on the chemical structure of the fluorophore and the environment it is in.

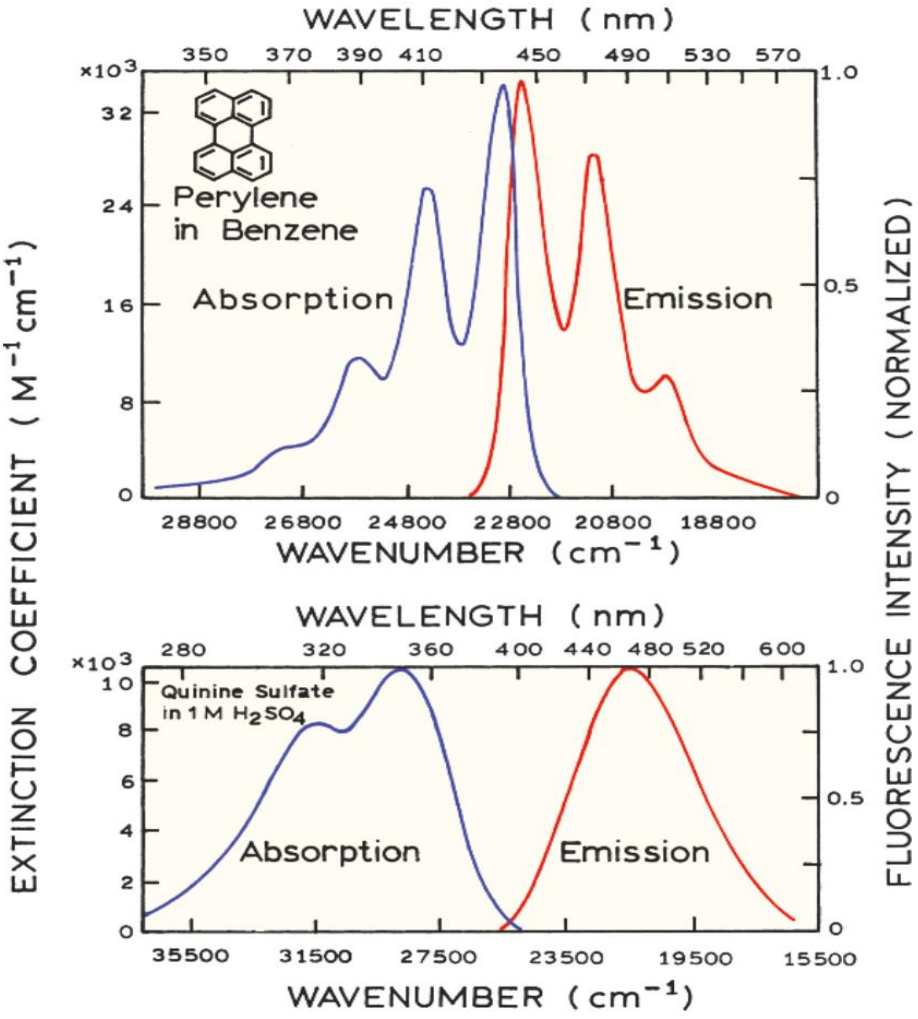

Figure 2 Absorption and emission spectra for perylene (up) ad quinine sulfate (down) [1].

Fluorescence is characterized by fluorescence lifetime and quantum yield. Molecules with the largest quantum yield, like rhodamines, display the brightest emissions. Quantum yield (Q) is the ratio of emitted photons to absorbed photons, and is given by

$$Q = \frac{\Gamma}{\Gamma + k_{nr}} \tag{1.1}$$

where Υ is emission rate and k_{nt} is non-radiative decay rate. Fluorescence lifetime also plays an important role in revealing emission information as it indicates the time required for fluorophores to interact with its environment. Fluorescence lifetime (τ) is given by

$$\tau = \frac{1}{\Gamma + k_{nr}} \tag{1.2}$$

When non-radiative processes are absent, the lifetime of a fluorophore is called the natural lifetime (τ_n) and is given by

$$\tau_n = \frac{1}{\Gamma} \tag{1.3}$$

In principle, the natural lifetime τ_n can be calculated from absorption spectra, extinction coefficient, and emission spectra of the fluorophore.

1.2 Fluorescence quenching

Fluorescent quenching is the phenomenon in which fluorescent intensity is reduced by various processes. Collisional quenching usually happens when an excited-state fluorophore is deactivated upon contact with a quencher. In this case, the fluorophore returns to the ground state during a diffusive interaction with the quencher. Examples of quenchers include oxygen, halogens, amines, and electron-deficient molecules like acrylamide. Different from collisional quenching, static quenching occurs when ground state fluorophores form non-fluorescent complexes with quenchers.

Quenching provides a valuable method to understand the role of excited-state lifetime in fluorescent measurements to detect dynamic processes in solutions. Absorption occurs in less than 10 ps, so it is an instantaneous event. So absorption spectroscopy only reveals information on the average ground state of molecules that absorb light and only molecules immediately adjacent to the absorbing species affect its absorption spectrum. However, emission occurs over a longer period of time so that it provides a chance for excited-state fluorophores to interact with other molecules in the solution. For example, collisional quenching of a molecule of lifetime of 10 ns by oxygen in water at 25 ºC gives 70Å total observant distance.

1.3 Approaches used to get fluorescence enhancement

There are several methods to enhance the fluorescence output. Metal-enhancement fluorescence (MEF) and nano-engineered surfaces were used to augment the excitation of fluorophores and provide directionality to the emitted light for improved collection [2]-[5].

1.3.1 Metal-enhanced fluorescence

The investigation of MEF began in the 1960s when Drexhage observed that a fluorescent molecule close to a metal film exhibits modified decay times and angular distribution of emission [3]. MEF can be attributed to three known mechanisms shown in Figure 3: (1) energy transfer quenching, k_m, from the fluorophore to metal with d^{-3} dependence; (2) increased emission due to concentration of local electromagnetic field E_m; (3) modification of the radiative decay rate of the fluorophore through local modification of the photon density of states [3].

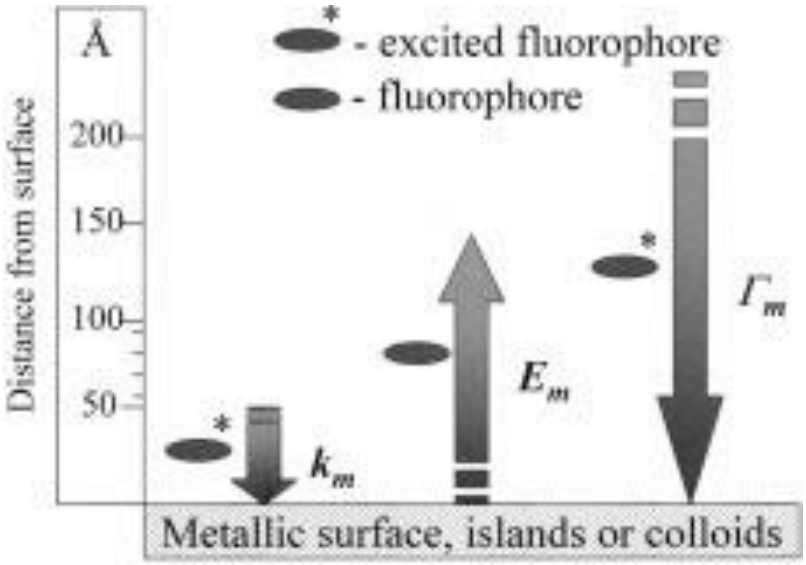

Figure 3 Predicted distance dependencies for a metallic surface on the transitions of a fluorophore. The metallic surface can cause Forster-like quenching with a rate k_m, can concentrate the incident field, E_m, and can increase the radiative decay rate, Γ_m [3].

We can use the Jablonski diagram in Figure 4 to better understand these third mechanisms.

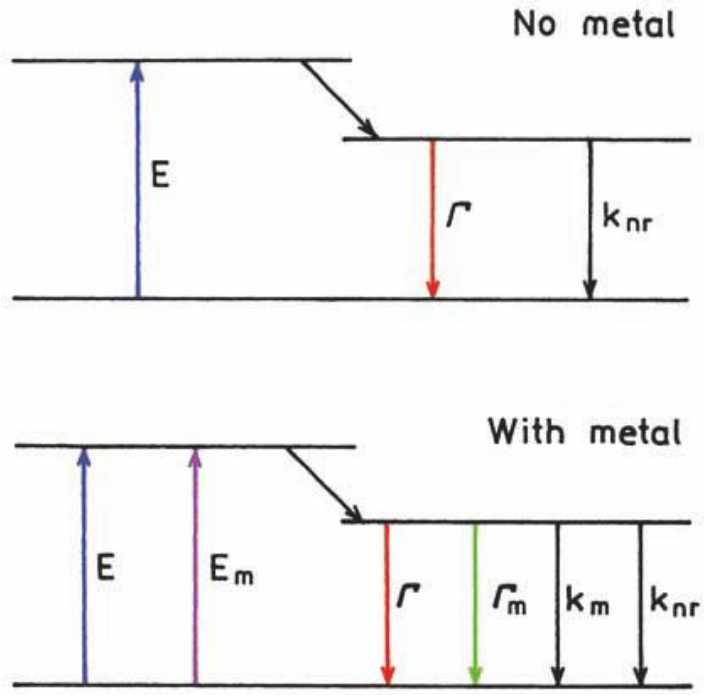

Figure 4 Jablonski diagram without (top) and with (bottom) the effects of near metal surfaces. E is the rate of excitation without metal. E_m is the additional excitation in the presence of metal [1].

For simplicity, only radiative decay (Γ) and non-radiative decay (k_{nr}) are considered. When there is no metal enhancement, the quantum yield and lifetimes are given by

$$Q_0 = \frac{\Gamma}{\Gamma + k_{nr}} \tag{1.5}$$

$$\tau_0 = \frac{1}{\Gamma + k_{nr}} \tag{1.6}$$

When metal is present, there is an increase in the radiative decay rate which raises quantum yield. The metal enhancement, the quantum yield and lifetimes near the metal surface are given by

$$Q_m = \frac{\Gamma + \Gamma_m}{\Gamma + \Gamma_m + k_{nr}} \tag{1.7}$$

$$\tau_m = \frac{1}{\Gamma + \Gamma_m + k_{nr}} \tag{1.8}$$

The effect of increasing Υ_m is shown in Figure 5. The x-axis is the ratio of radiative decay rate due to metal and the rate in absence of metal. As Γ_m increases, the lifetime decreases which is mostly due to increases in k_{nr}. When the total decay rate $\Gamma_T = \Gamma + \Gamma_m$ increases, the quantum yield increases because

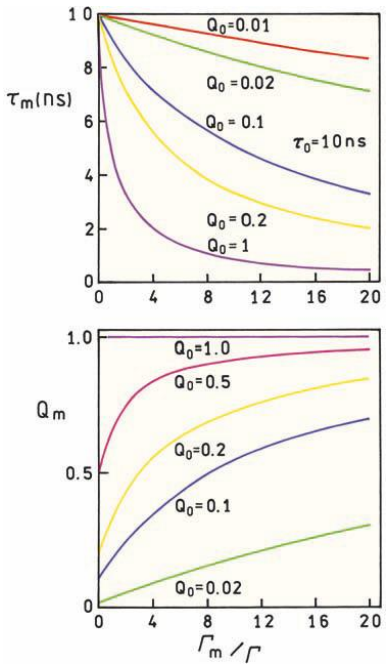

Figure 5 Effect of an increase in the metal-induced radiative rate on the lifetime and quantum yields of fluorophores [2].

more fluorophores emit before they decay non-radiatively. For fluorophores with lower quantum yield, the enhancement effect is larger.

A variety of MEF have been implemented to enhance fluorescent output since 1980s. Pompa et al. [4] developed arrays of gold nanostructures coupled to CdSe/ZnS nanocrystals dispersed in a polymer blend. Their method achieved ~30-fold fluorescence enhancement and demonstrated the possibility of obtaining precise control and a high spatial selectivity of the fluorescence enhancement process [4]. Kinkhabwala et al. fabricated a gold bowtie nanoantenna surface to achieve a factor of ~1350 fluorescent enhancement near the sharp metal tip [5].

2. Photonic Crystal Fluorescence Enhancement

The Cunningham Group at the University of Illinois has demonstrated that a periodic nano-structure photonic crystal (PC) is capable of enhancing fluorescent output by more than x8000 [6]. While MEF focuses on modification of radiative decay rate of fluorophores in close proximity to a metal surface to achieve enhanced output, photonic crystal enhanced fluorescence (PCEF) utilized the effect of resonant optical coupling to achieve enhanced excitation and enhanced extraction. Compared to MEF, PCEF is preferred for biological assay for the following reasons: 1) PCEF's higher enhancement factor and signal-to-noise ratio (SNR) are ideal for low concentration biomarker detection; 2) PCEF is free of the quenching effect that exists on lossy metal surfaces; 3) PCEF surface can be mass produced inexpensively using a variety of materials [6,7].

2.1 PC explained

PCs are composed of periodically refractive index modulated nano-structures which can be divided into three broad classes: one-dimensional (1D), two-dimensional (2D) and three-dimensional (3D), shown in Figure 6. The defining feature of a PC is the periodicity of a dielectric material along one or more axes.

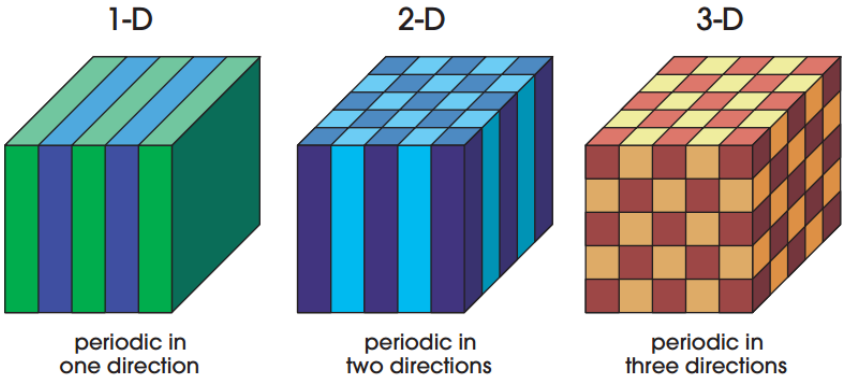

Figure 6 Example of 1D, 2D, 3D photonic crystals. Different colors indicate material with different refractive index [8].

PCs modulate light propagation similarly to semiconductors. By engineering the periodic dielectric function to construct photonic band gap, light can be confined in certain directions with specific frequencies by refraction and reflections of light from various media [8]. Bragg mirrors which produce ultra-high reflectivity (~99.999%) and the patterns on butterfly wings are examples of 1D and 2D PCs.

2.1.1 Optical resonance in PCs

Here we study the 1D PCs comprised of a low refractive index periodic surface grating coated with a high refractive index dielectric thin film. These PCs belong to a subset of diffractive optical elements (DOE) which modify wavefronts by segmenting and redirecting segments via interference and phase control. Under certain conditions, uneven distribution of light can exist, called “anomalies” by R. W. Woods who first discovered these effects in 1902 [9]. The effects are categorized into two groups: Rayleigh anomalies and resonance anomalies.

Rayleigh anomalies occur at the frequency where scattered light emerges tangentially to the grating surface [10]. And the position of Rayleigh anomaly is given by the grating equation:

$$\sin\theta_n = \sin\theta + \frac{n\lambda}{\Lambda} \tag{2.1}$$

where θ is the incident angle , θ_n is the diffraction angle, λ is free space wavelength and Λ is grating period. From Equation 2.1, anomaly spectral position for a given incident angle is given by:

$$\lambda = \frac{\Lambda}{n(-\sin\theta \pm 1)} \tag{2.2}$$

Resonance anomalies were initially studied in metal grating and are caused by surface excitation effect [10]. In dielectric structures with periodic index variation (i.e., dielectric-waveguide grating and photonic crystal slab), the anomalies are able to cause guided-mode resonances (GMR) such that optical energy can be switched between 100% reflected and 100% transmitted. Figure 7 shows an example of GMR in photonic slab.

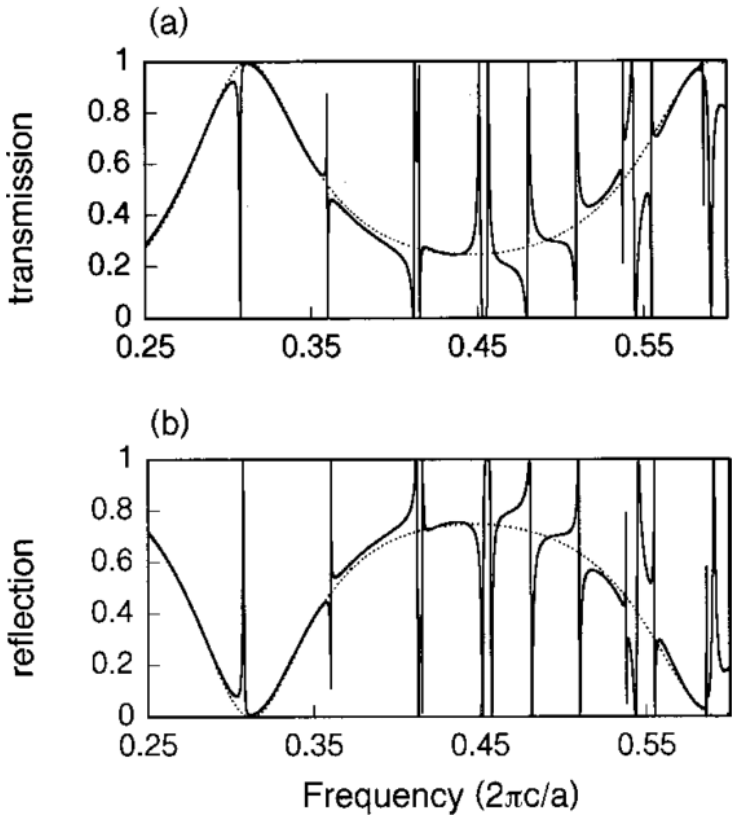

Figure 7 (a) Transmission and (b) reflection spectra. The solid lines are for the photonic slab structure shown in Fig. 2(b). The dashed lines are for a uniform dielectric slab with a frequency-dependent dielectric constant and thickness same as Fig. 2(b) [11].

This thesis focuses mainly on GRMs in 1D PCs for enhanced fluorescence. The physics of 1D PC upon plane wave incidence can be understood by the ray picture model. Figure 8 shows a simple 1D PC made up of a substrate with patterned wave confinement layer on top.

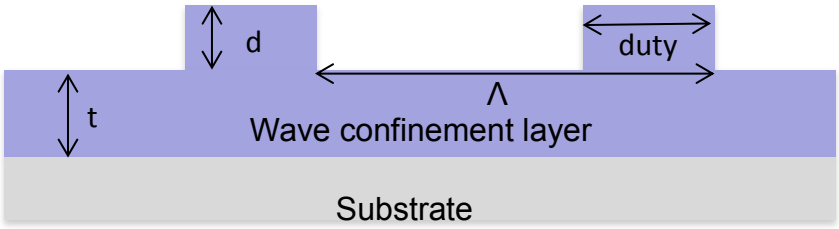

Figure 8 1D PC schematic.

When this structure is illuminated by a plane wave, some of the wave gets transmitted out directly through the structure, while a part gets diffracted by the grating and is trapped in the wave-confinement layer. This re-diffracted trapped wave couples out of the wave-confinement layer in both forward and backward directions so that it interferes both with the reflected part and the transmitted part of the wave. 1D PC resonates at a specific wavelength and angle of incidence when complete destructive interference occurs with the transmitted light, so no light is transmitted through the structure. If there is complete construction interference in reflected light, all the light is reflected, therefore a sharp reflection peak is observed in far-field reflection spectrum or an ideal PC without any defects or structure misalignment, so the reflection peak is 100% (Figure 9). There are two incident polarization directions used in this thesis: transverse electric (TE) and transverse magnetic (TM). TE polarization has the polarization pointing along the grating. TM polarization has polarization pointing perpendicular to the grating direction in 1-D PCs.

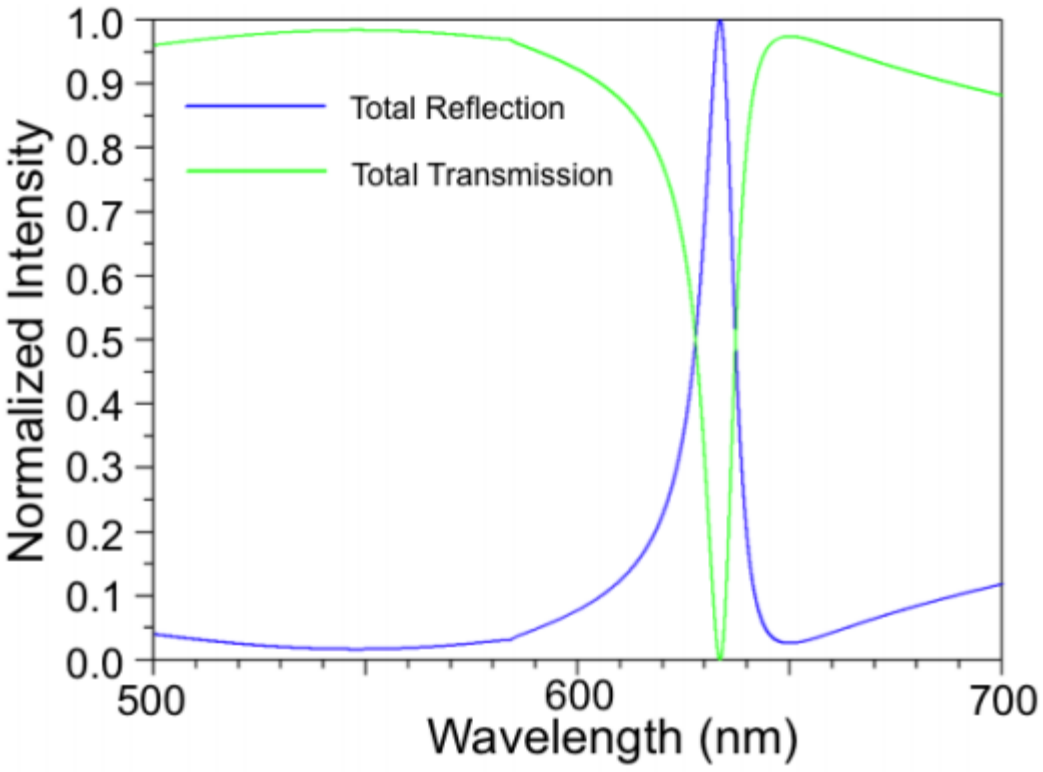

Figure 9 Simulated total reflected and transmitted power for the PC shown in Fig. 5 for a TM polarized light shining normally on the surface. At resonance wavelength, 100% of the incident light is reflected back resulting in no transmission at that wavelength [13].

2.1.2 Ray picture model

This section utilizes the simple ray model analysis proposed by Sharon et al. [12] to understand GMRs in 1D PCs. The resonant guided waveguide is comprised of a substrate, a waveguide layer, and a grating layer as shown in Figure 10. Upon plane wave illumination, at location A, part of the ray undergoes 0^{th} order diffraction and ends up as transmitted ray t, while the rest of it undergoes 1^{st} order diffraction that is confined in waveguide under phase matching condition :

$$n_1 k \sin\theta \pm mK = n_3 k \cos\varphi \qquad (2.3)$$

where $k=2\pi/\lambda$ is free space wavevector, m is the order of diffraction, $K=2\pi/\Lambda$. Λ is grating period and φ is internal diffraction angle. One can engineer the grating period so that when the 1^{st} order diffracted light

arrives at D, some of it gets re-diffracted and transmitted through waveguide layer and ends up in substrate layer (marked as s), while the rest is reflected back into the wave-confinement layer and propagates as its resonant mode and the above cycle is repeated[13]. For such an asymmetric wave-confinement slab, the propagating guided-mode of order m should satisfy the following phase condition:

$$2k_3 d + 2\phi_{13} + 2\phi_{34} = 2m\pi \quad (2.4)$$

Here $k_3 = n_3 \sin\varphi$ is the wavevector of light in the z direction in the wave-confinement layer. $\Phi 13$ is Fresnel shift by medium 1 and 3, and ϕ_{34} is the Fresnel shift by medium 3 and 4. If Equation 2.4 is satisfied, trapped light will bounce back and forth within the wave-confinement layer, resulting in a single wave that propagates as a guided mode in the layer [13].

On the transmitted side, ray t interferes with ray s. The phase difference, Φ, between t and s comes from the phase shifts caused by diffractions, total internal reflection and the difference in optical paths between these two rays shown in Equation 2.5 [12].

$$\phi = \phi_{path} + \phi_r + \phi_d \quad (2.5)$$

Optical path difference (ϕ_{path}) can be calculated using the following simplified conditions: we draw a wavefront for the incident ray at point A (shown as u in blue). Consider a point F on that wavefront such that the incident ray originating from F will hit the grating at a point B, where the distance between A and B is pΛ, with p being an integer[13].

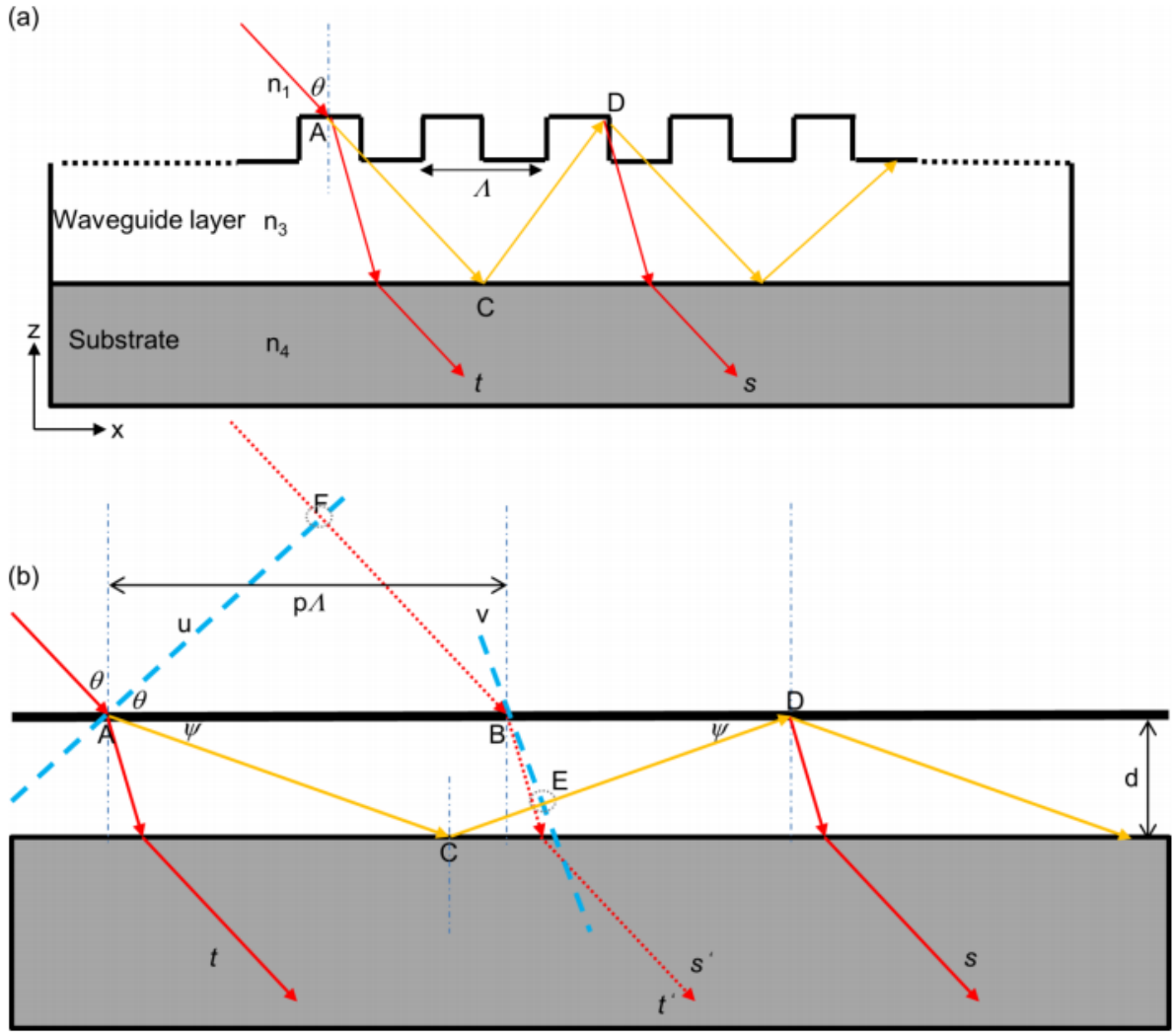

Figure 10 Schematic showing paths of various rays when a TE polarized light is incident at an angle θ on a 1-D PC. The transmitted rays are labeled as t and s. b) Geometry for computing the optical path difference between rays t and s. The wavefronts at point A and E are marked in dashed blue [13].

Then let us draw a wavefront on ray CD that will also intersect the grating at point B. This gives the same starting points for the two transmitted rays marked as t' and s'. The path difference between t' and s' is calculated as ACE-DE and BF. ACE-DE is the distance travelled by light in the wave-confinement layer before it hits point B. BF is the distance travelled by incident light in the superstrate before it hits B. Thus the optical path difference between t' and s' is:

$$\begin{aligned} \Delta &= n_3(ACD - DE) - n_1 BF \\ &= n_3\left(\frac{2d}{\sin\varphi} - \cos\varphi\left[\frac{2d}{\tan\varphi} - p\Lambda\right]\right) - n_1 p\Lambda\sin\theta \\ &= n_3(2d\sin\varphi + \cos\varphi\, p\Lambda) - n_1 p\Lambda\sin\theta \end{aligned} \tag{2.6}$$

Using phase matching condition, the above can be reduced to

$$\Delta = 2dn_3\sin\varphi + \frac{mp2\pi}{k} \tag{2.7}$$

Then the optical phase difference due to paths is

$$\phi_{path} = k\Delta = 2dn_3\sin\varphi + mp2\pi = 2dk_3 d + mp2\pi \tag{2.8}$$

The phase difference caused by total reflection is:

$$\phi_r = 2\phi_{34} \tag{2.9}$$

The phase difference caused by diffractions at point A and caused by classical diffraction and Fresnel phase shift due to refractive index contrast between layers 1 and 3 is

$$\phi_d = \phi_{13} + \frac{\pi}{2} \tag{2.10}$$

Thus, by adding all the phases, we finally get to the phase difference between rays t and s as:

$$\begin{aligned} \phi &= \phi_{path} + \phi_r + 2\phi_d \\ &= 2k_3 d + 2\phi_{34} + 2\phi_{13} + \pi \end{aligned} \tag{2.11}$$

Using Equation 2.8, Equation 2.11 can be reduced to

$$\phi = 2m\pi + \pi \tag{2.12}$$

So we observe that at resonance condition, transmitted and diffracted wavefronts that are completely out of phase give 0% transmitted power or 100% reflection [13].

2.2 Photonic crystal enhanced fluorescence

The PC mainly provides amplified fluorescent output through two mechanisms: enhanced excitation and enhanced extraction.

2.2.1 Enhanced excitation

Enhanced excitation is the phenomenon in which, when resonant excitation (incident wavelength, polarization and angle) for the PC is reached, the intensity of emission from the fluorophores will be greatly enhanced if they are placed within the evanescent field and have an absorption spectrum that matches the PC resonant wavelength. Fundamentally, enhanced excitation is caused by enhanced absorption rate of fluorophores upon the PC surface. It was shown previously that TM polarization results in narrow linewidth with higher Q factor, so TM resonance is preferred to TE resonance for the same device. Enhanced excitation works selectively within evanescent field and has average decay length ~ 85nm [14]. Decay length is approximately linearly proportional to resonance wavelength in the wavelength range with low dispersion. Figure 11 shows the effect of enhanced excitation for PPL-ALEXA 647 fluorophores on glass compared to a quartz PC surface. This quartz PC reaches an enhancement factor of 686x and 330x SNR improvement [15].

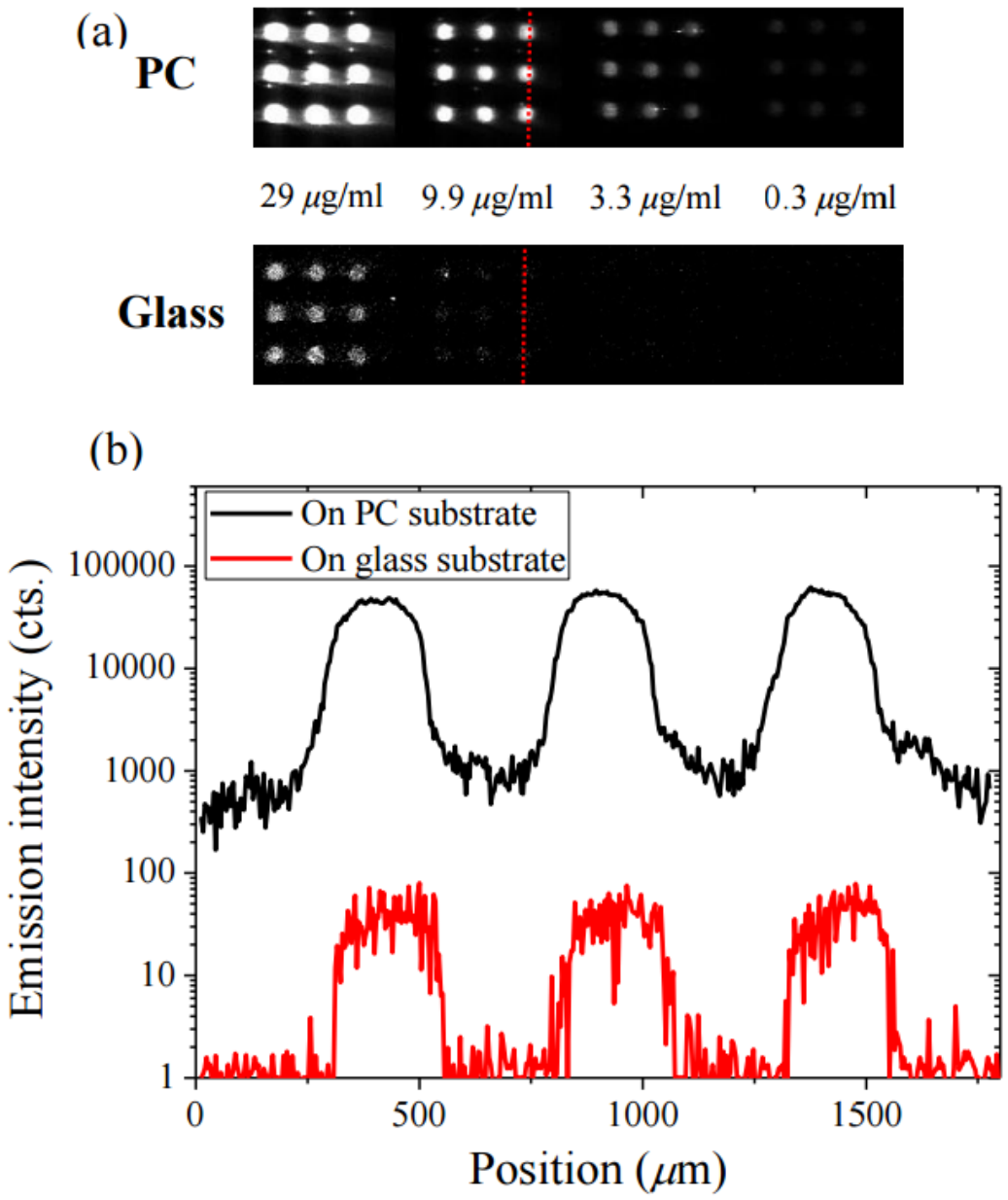

Figure 11 (a) Gain and exposure-optimized images of PPL-Alexa 647 fluorescence on glass compared the PCEF surface; (b) Intensity profile as a function of distance for line of fluorescent image pixels profiling spots of concentration 9.9 μg/ml on both glass and the PCEF surface [15].

2.2.2 Enhanced extraction

Enhanced extraction is the phenomenon in which the emission from fluorophores near the PC surface can couple to one of the resonant modes of PC and then emerge out in an angle-dependent fashion. This provides us a method to engineer the surface so that emission can be collected with much higher sensitivity. As mentioned in 2.1, guided-mode resonance for a 1D PC is governed by phase matching into and out of the high refractive index layer:

$$k_0 n_s \sin\theta \pm \frac{m2\pi}{\Lambda} = \beta \tag{2.13}$$

where m is diffraction order, Λ is period, β is real part of propagation constant resonant mode, k_0 is free-space wave-vector, and n_s is refractive index of the medium from which the light is incident at an angle θ with the surface normal of the PC.

Conversely, radiation produced by fluorophores in close proximity to the device not only directly emits into the substrate and superstrate regions, but also couples to a leaky mode and can be extracted along its dispersion. Using equation 2.13, angle of escape can be calculated as:

$$\sin\theta = (\beta \pm \frac{m2\pi}{\Lambda}) k_0 n_s \tag{2.14}$$

This implies that for arbitrary wavelength of coupled light, angle of escape can be arbitrarily chosen by appropriate design of the PC. Equation 2.14 also implies that light can be extracted symmetrically about surface normal in both superstrate and substrate regions [16].

Figure 12 shows angle-dependent fluorescence extraction for a 1D PC, and Figure 13 shows the enhanced emission for quantum dots (QD) integrated in a PC

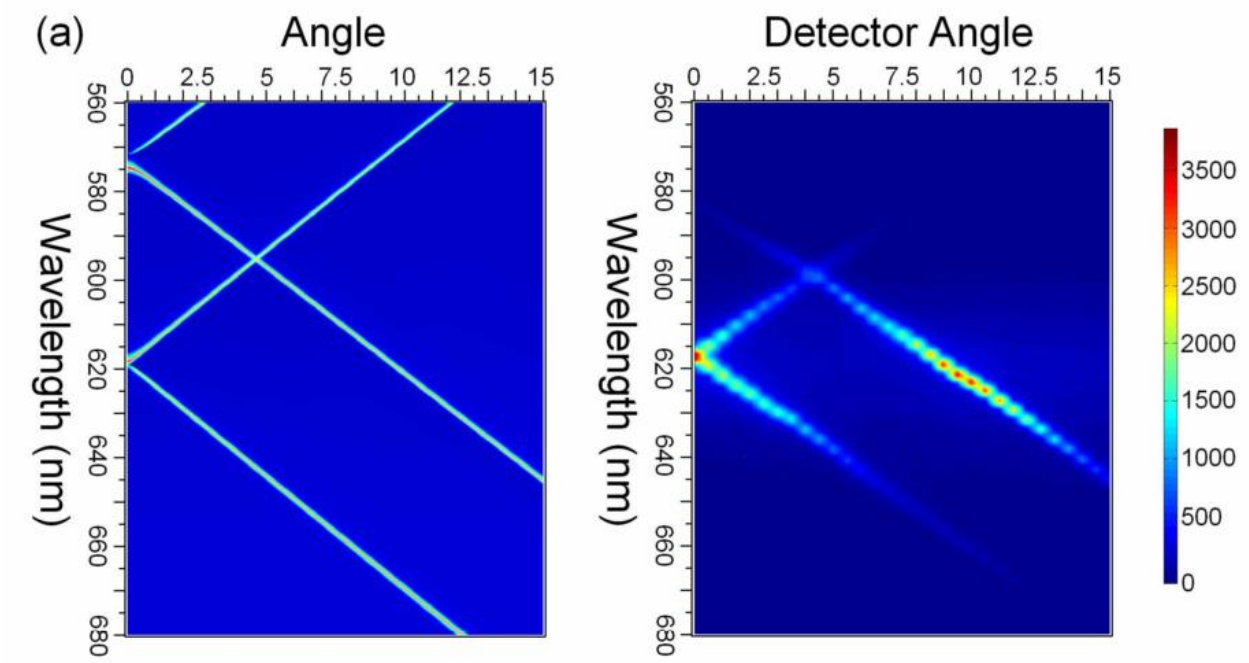

Figure 12 Leaky mode dispersion and angle-resolved fluorescence. Comparison between the RCWA calculated leaky mode dispersion and the resonant features in the angle-resolved fluorescence measurements for the (a) linear [16].

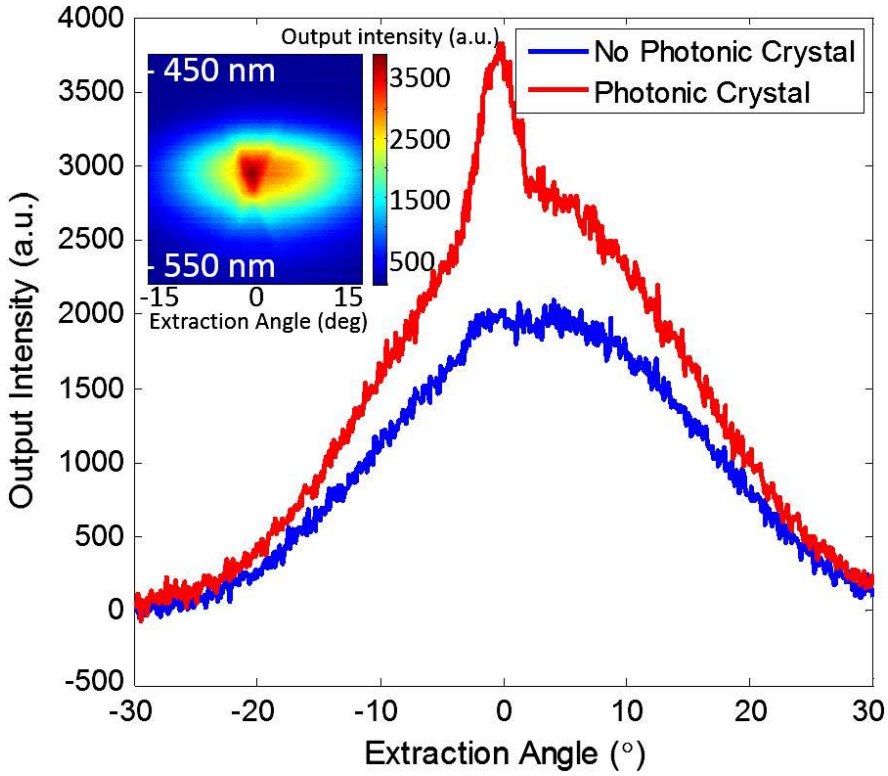

Figure 13 Impact of angle on QD extraction measured with and without a PC structure present [17].

3. Mirror-underneath PC for Further Enhanced Fluorescence Emission

3.1 Introduction

As shown previously, PCEF technology has been employed for biomarker detection, disease diagnosis and monitoring biological processes for its high signal enhancement and high SNR. In order to get higher PCEF, one can focus on improving enhanced excitation through better dimension control of the PC, and on improving the coupling efficiency of fluorescent emission to far field. This chapter reviews the past work focusing on coupling PC resonance to a Fabry-Perot cavity on quartz substrates and discusses current work on transferring it to silicon substrates. Specifically, we focus on simulation and design, tolerance analysis, fabrication, and device characterization. Lastly, we demonstrate that the new PC provides 10x increase in SNR compared to ordinary PC through experiments to detect dye-tagged proteins. This shows a promising method to improve the limit of detection of fluorophore-tagged biomarkers, thus benefiting early disease prevention, diagnostics and monitoring.

3.2 Mirror-underneath PC explained

The effects of placing a mirror under the PC grating are as follows: First, the mirror layer reflects fluorescence emission from the PC surface that would normally be directed downwards, resulting in 2x increase in photon detection. Second, we can engineer the length between PC gratings and the mirror so that it establishes a Fabry-Perot cavity, in which constructive interference occurs. Thus 3-5x more electric-field intensity enhancement can occur from the coupling of the PC and Fabry-Perot cavity.

3.3 Past work on PC coupled to an optical cavity

Pokhriyal et al. [18] fabricated a plastic based PC coupled to an optical cavity that demonstrated better SNR than an ordinary PC. Figure 14 shows cross section schematics of the PC and cavity-coupled PC experimented on in [18]. The PC is made from patterned SU8 polymer with TiO_2 film on top. For the cavity-coupled PC, there is a gold mirror inserted between silicon and SU8 which results in higher evanescent fields on the PC surface by coupling the PC mode to the Fabry-Perot cavity.

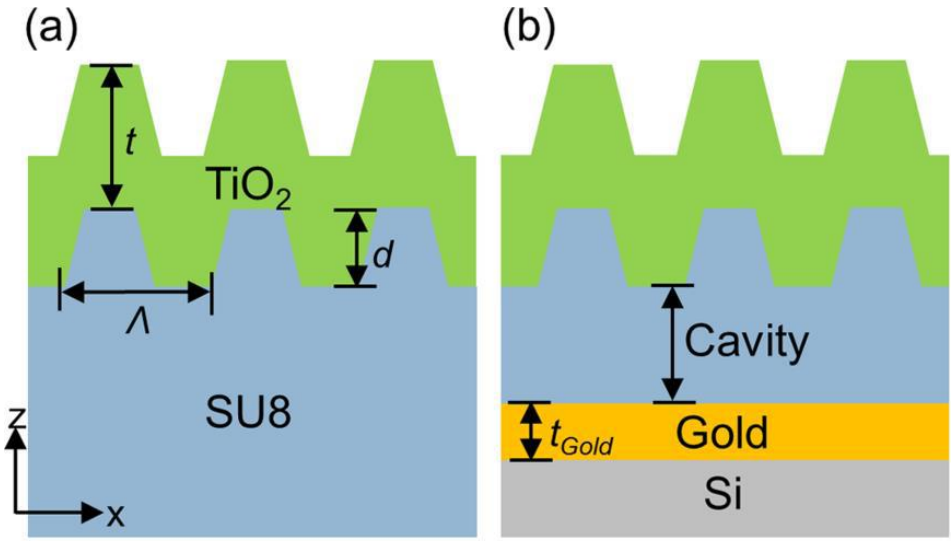

Figure 14 Cross-sectional schematic (not to scale) of the PC (a) compared to the cavity-coupled PC (b) [18].

3.4 A silicon-based PC coupled to optical cavity

Making PCs on silicon substrates has the advantage of better device fabrication control through a well-established standard semiconductor process. Besides, it opens the chance to combine optical and electronic technology on an integrated circuit. Thus, it is beneficial to develop future PCEF substrates on silicon for its low cost and high volume production. Besides, lower concentration of analytes detection can be achieved because silicon based PC has lower autofluorescence or noise.

3.4.1 Material selection and simulation

Here we implement a novel approach for further increasing the fluorescence enhancement factor by placing a mirror underneath the ordinary PC structure. After consulting the foundry service (Novati Technologies, Inc.) which will produce the designed device, we identified three materials—titanium, aluminum, and titanium nitride—for their availability and relatively low costs.

Rigorous coupled wave analysis (RCWA) electromagnetic simulations (RSOFT, Inc.) are performed to aid with mirror material selection. We focus on selecting the material that provided a reflection dip at 637 nm with narrowest full width at half maximum and maximized field enhancement.

The structure we simulate is shown in Figure 15 which comprises a silicon substrate (thickness = 2mm) with a mirror layer material (thickness = 100nm), silicon dioxide cavity layer (thickness = 216nm), patterned silicon dioxide (λ= 360 nm, duty cycle = 33%, cavity length = 205nm, grating height = 80nm) and a titanium dioxide (thickness = 125nm) layer on top. The refractive indexes of the three materials that we simulate with are shown in Table 1.

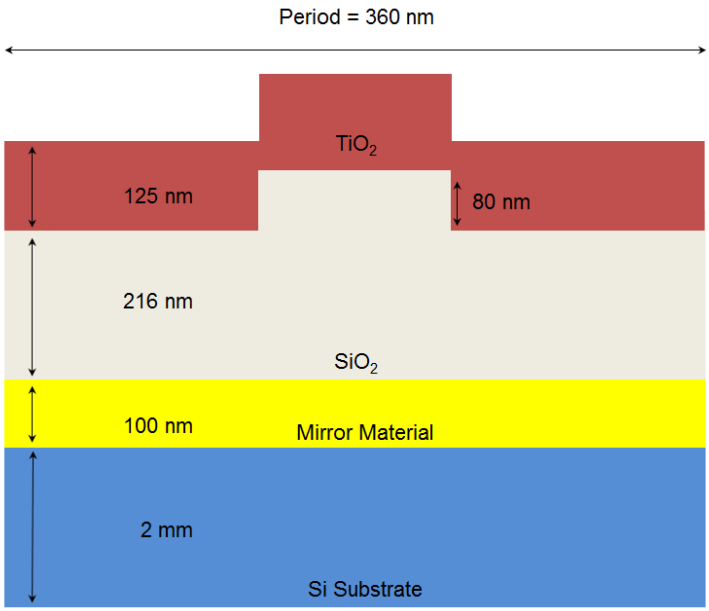

Figure 15 Cross section of structure simulated (not to scale).

Table 1 Complex refractive index of aluminum, titanium and titanium nitride at 637nm

	Real part of refractive index	Imaginary part of refractive index
Aluminum	1.398	7.457
Titanium	2.166	2.938
Titanium Nitride	0.860	2.4963

Simulated far-field spectra of normal incidence with TM polarization are shown in Figure 16 which shows that the aluminum-mirror-underneath PC, titanium-mirror-underneath PC, and titanium nitride-mirror-underneath PC all have reflection dips near 637 nm. However, the aluminum-mirror-underneath PC has the best performance because its full-width-at-half-maximum is the narrowest (3 nm), and its reflection is the lowest (1.3%). This indicates the strongest coupling of light and the aluminum-mirror-underneath PC.

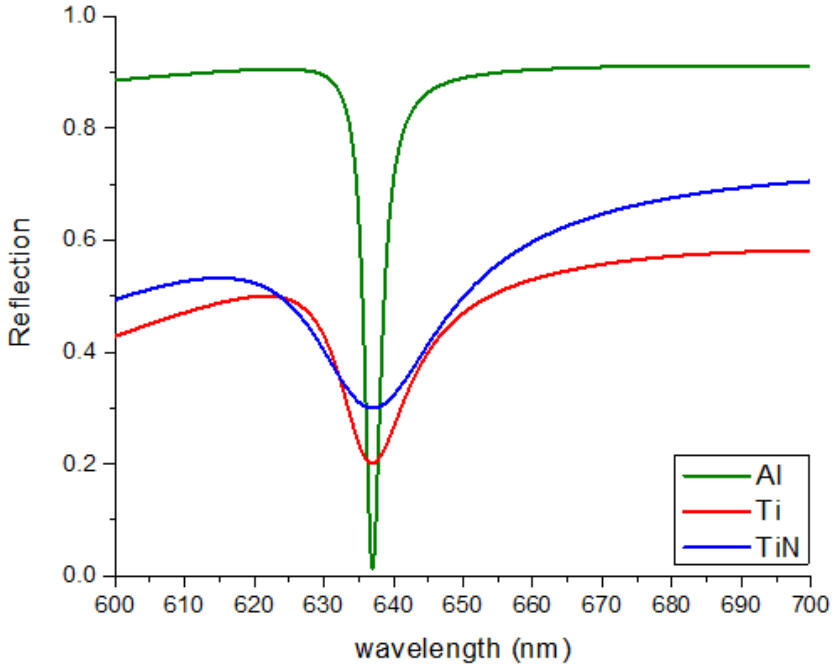

Figure 16 Simulated far-field spectra of the mirror-underneath PC using Al, Ti, and TiN as mirror layer respectively.

Like the ordinary PC mentioned in chapter 2, resonance for the mirror-underneath PC also depends on both the incident angle and incident wavelength. Figure 17 shows the simulated band diagram (θ = 0° to 10°) for the mirror-underneath PC device show in Figure 15 with aluminum as mirror layer. Here θ is the angle between the incident beam and the grating's normal vector in the plane perpendicular to the grating direction. It is easy to see from the figure that resonant wavelength is very sensitive to θ.

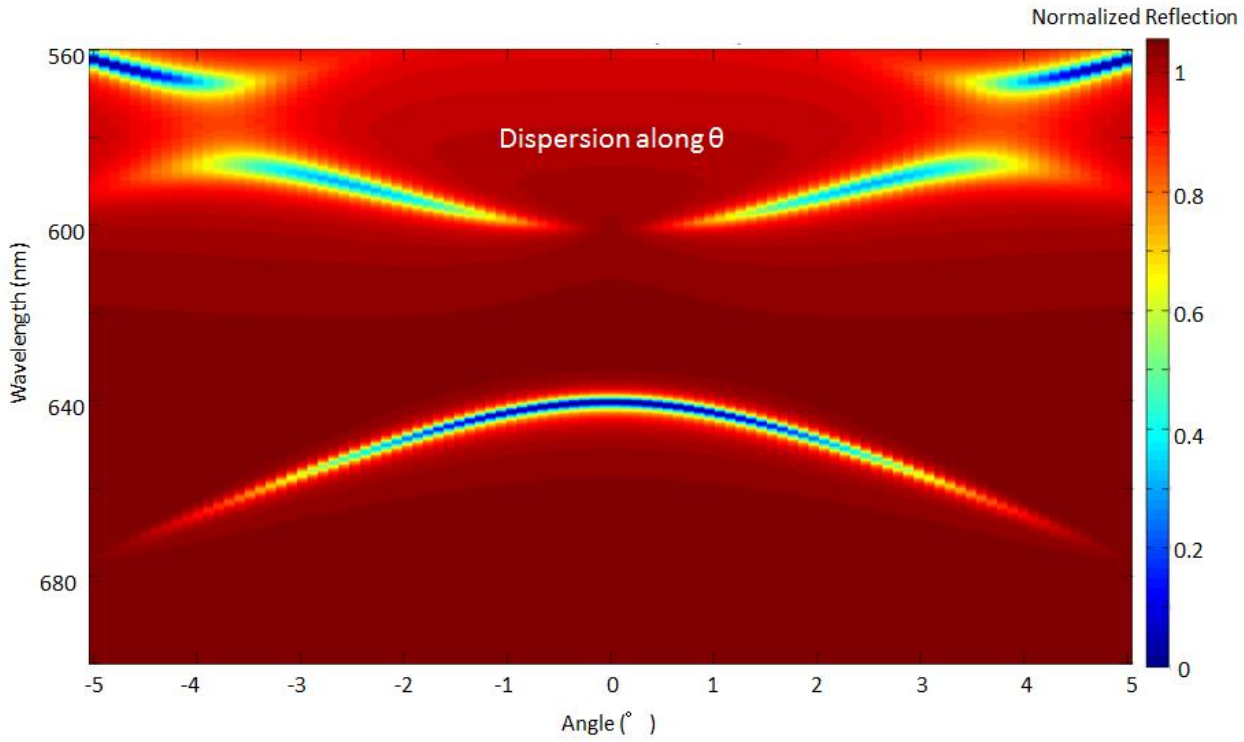

Figure 17 Simulated photonic band diagram of the mirror-underneath PC with θ varied from 0° to 10°.

Next, we perform near-field distribution simulation for one period of each PC. The incident light wavelength is set to be 637nm at normal incidence with TM polarization. Figures 18 to 20 show the simulated near-field intensity distribution for each PC. It is clear to see from the figures that the aluminum-mirror-underneath PC offers the highest intensity distribution. We calculate the maximum enhancement factor and average enhancement factor shown in Table 2. Here the enhancement factor (enhancement factor) is defined as

$$EF = \frac{|E|^2_{PC\ surface}}{|E|^2_{non-PC\ surface}} \tag{3.1}$$

Since the PC enhancement is a near-field effect that is localized to the vicinity of the sensor surface, the average enhancement factor is calculated within a 30 nm region above the surface.

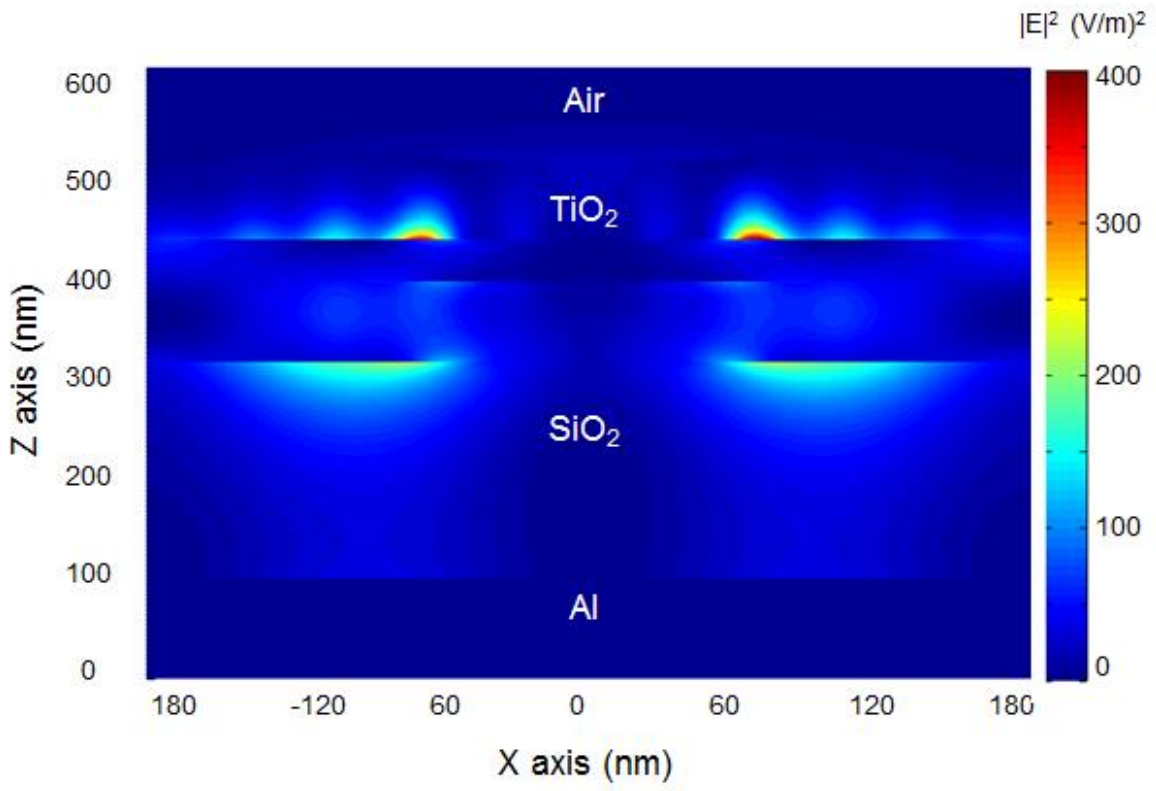

Figure 18 Near-field electric field intensity distribution for the Al-mirror-underneath PC.

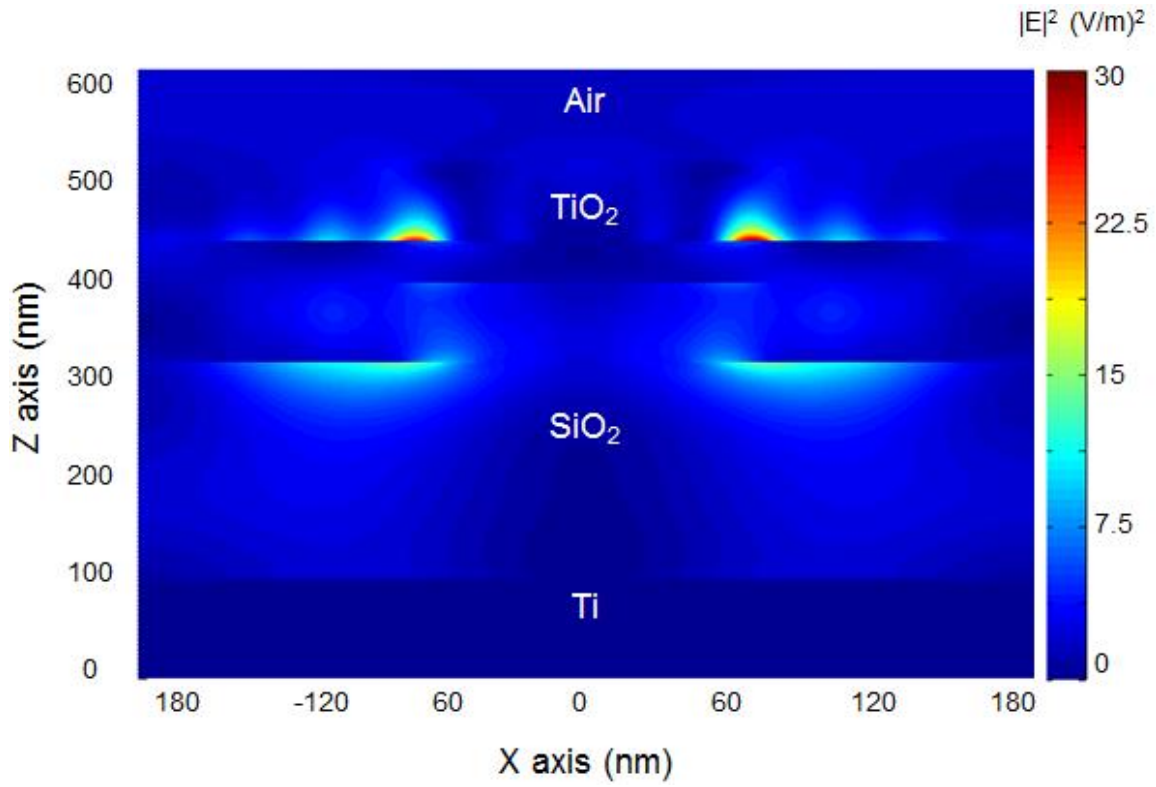

Figure 19 Near-field electric field intensity distribution for the Ti-mirror-underneath PC.

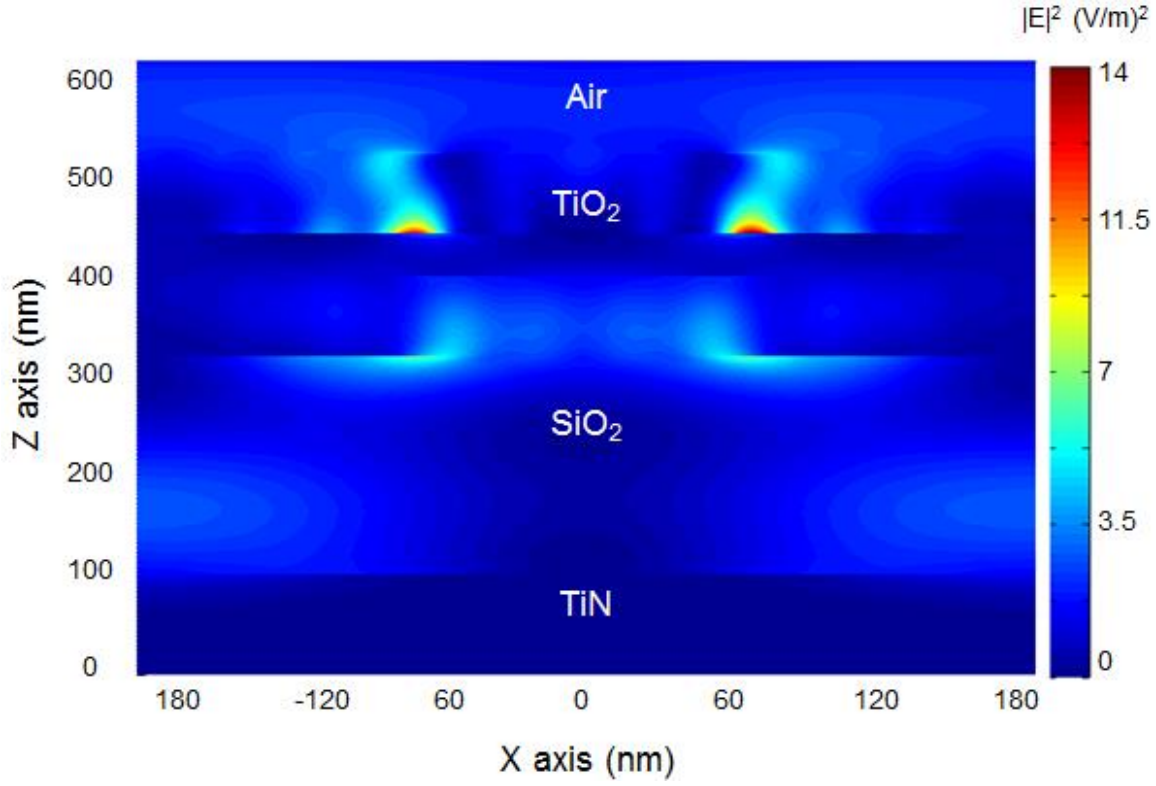

Figure 20 Near-field electric field intensity distribution for the TiN-mirror-underneath PC.

Table 2 Electrical field enhancement factors of mirror-underneath PC using three materials and of ordinary PC without mirror.

	Maximum enhancement factor	Average enhancement factor
Al mirror	422	88
Ti mirror	33	13
TiN mirror	15	12
No mirror	29	10

From the simulation and enhancement factor calculation, we decide that aluminum will be used as the mirror layer material as it provides the highest enhancement of near-field electric field.

3.4.2 Al-mirror-underneath PC tolerance analysis

Because there are fabrication unreliability and experimental setup mismatch in the actual experiment, this section studies the parameters that will affect the performance of the Al-mirror-underneath PC.

First we consider what will happen to the reflection spectra if cavity thickness (t_{cavity}), grating height ($h_{grating}$), titanium oxide thickness (t_{TiO2}) and incident angle (θ) deviate from ideal conditions. The reflection spectrum reveals information about coupling between PC-resonance and Fabry-Perot cavity. The Al-mirror-underneath PC cross section under this analysis is shown in Figure 21.

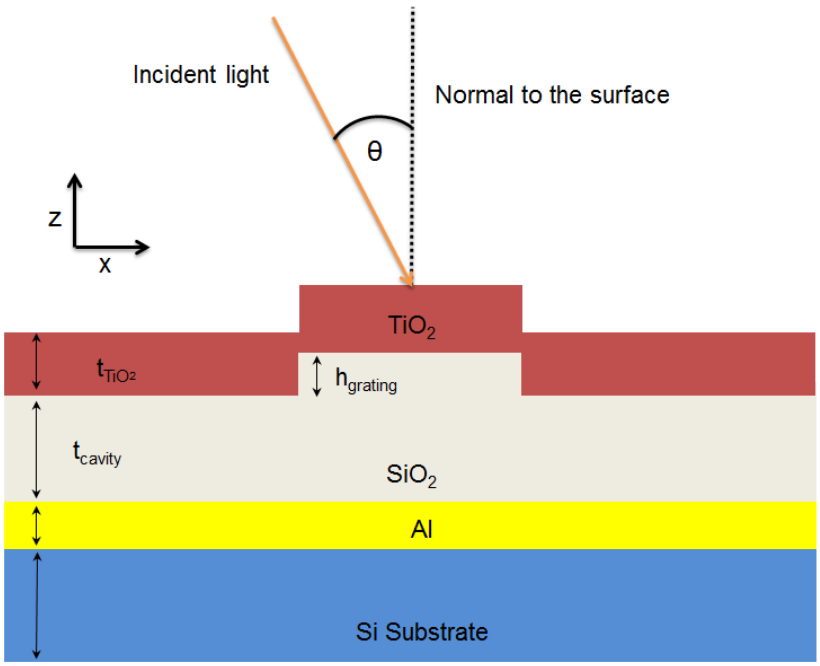

Figure 21 Schematic of Al-mirror-underneath PC under analysis.

Figure 22 (a-d) show simulated far-field spectra for varying parameters mentioned previously. The thickness deviation range is 10 nm with 1 nm step, and angle deviation is 10° with 1° step. The trend of reflection dip is summarized as follows:

1) As titanium oxide layer increases, reflection dip wavelength increases and reflectance increases.
2) As incident angle increases, reflection dip wavelength increases and reflectance increases.
3) As grating height layer increases, reflection dip wavelength decreases and reflectance decreases.
4) As cavity increases, reflection dip wavelength decreases and reflectance increases.

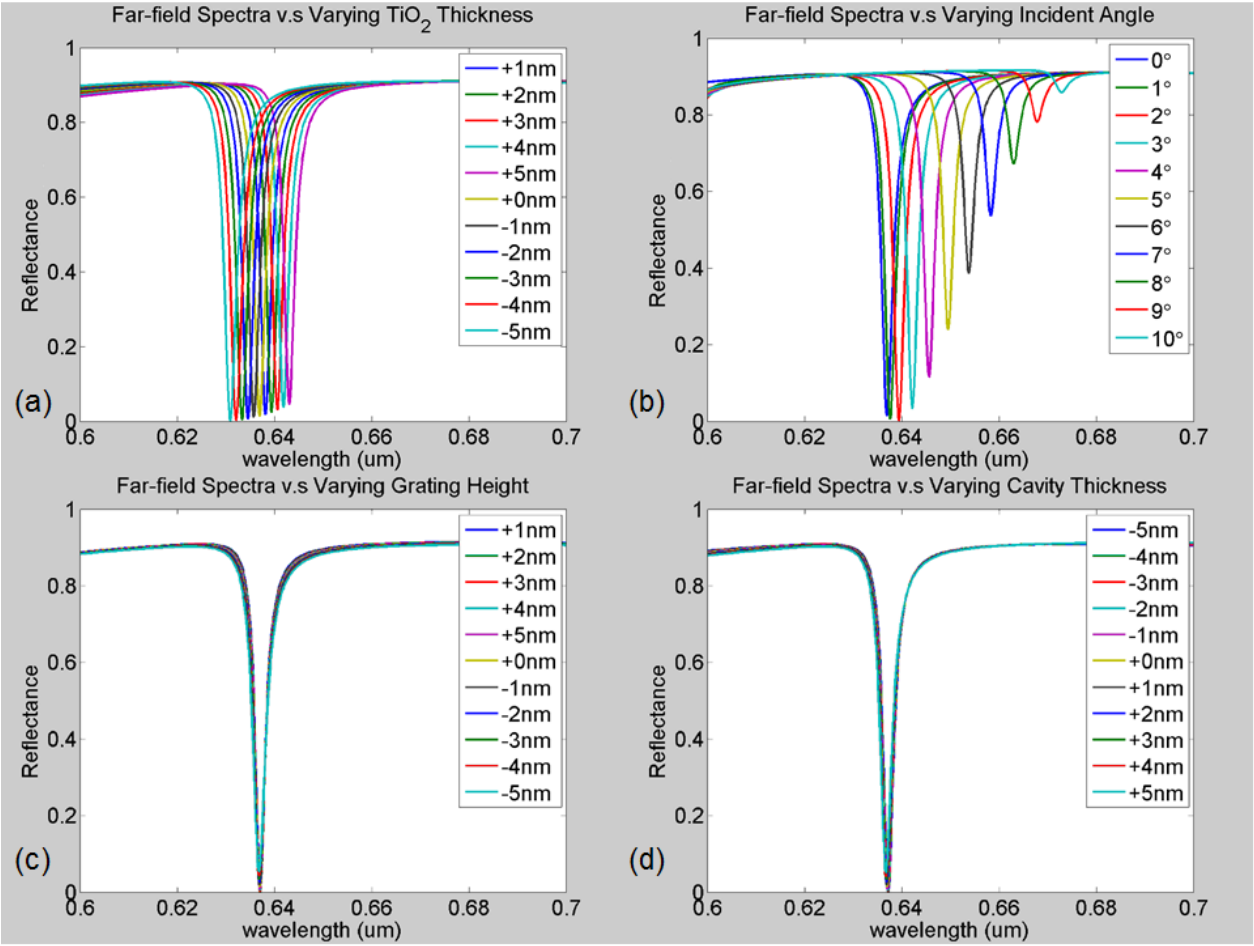

Figure 22 Simulated far-field reflection spectra for (a) varying TiO_2 thickness, (b) varying incident angle, (c) varying grating height, (d) varying cavity thickness.

We can see that grating height deviation or cavity thickness deviation does not cause significant reflection spectra change. But the device is very sensitive to TiO_2 thickness and incident angle. For every 1 nm titanium oxide thickness increase, the reflection dip wavelength red-shifts 1.2 nm with negligible reflection efficiency change; for every 1° angle increase, the reflection dip wavelength red-shifts 3.74 nm and reflection efficiency increases by 9%. Figure 23 plots the reflection dip wavelength when TiO_2 thickness and incident angle are away from resonant condition.

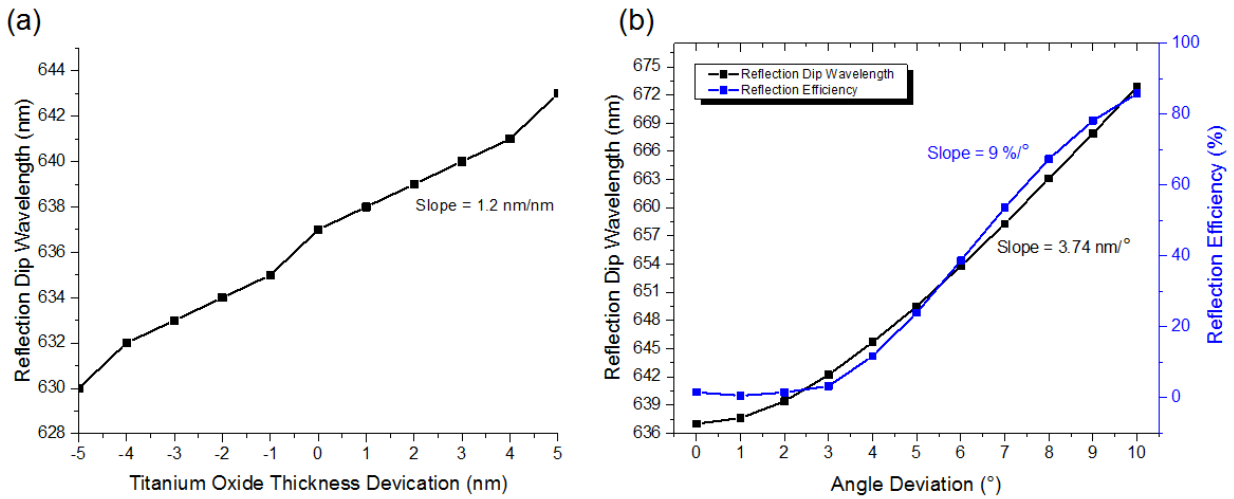

Figure 23 (a) Reflection dip wavelength when TiO_2 thickness deviates by -5 nm to 5nm from designed thickness and slope; (b) Reflection dip wavelength when incident angle deviates by 0° to 10° from normal incidence and its slope.

Since TiO_2 thickness and angle deviation can cause relatively large spectral shifts, it is wise to know whether one can tune the angle to regain resonance to 637nm with good enhancement factor when TiO_2 thickness is off by a few nanometers. Figure 24 (a) plots the reflection spectrum when TiO_2 layer is 10 nm less than ideal thickness: the green curve is the reflection spectrum at θ = 0° excitation, and shows a reflection dip at 625nm. In order to regain resonance wavelength (637 nm), one needs to tune the excitation angle. Figure 24 (b) shows the angle spectrum at 637 nm excitation. And it shows that θ = 4.53° excitation results in the lowest reflection, indicating 637 nm excitation is well coupled with the mirror-underneath PC. This can be seen from the reflection spectrum at θ = 4.53° excitation (blue curve) in Figure 24 (a) where the reflection dip wavelength now shifts to 637 nm. Although reflection increases from 0% to 34% in Figure 24 (a), at θ = 4.53° incidence the mirror-underneath PC still has higher enhancement factor. At θ = 4.53° excitation, the component of light that travels in normal direction (-z) is well coupled to the mirror-underneath PC grating and Fabry-Perot cavity. Table 3 shows the calculated enhancement factors for θ = 0° excitation and θ = 4.53° excitation at same excitation wavelength, 637 nm, for the mirror-underneath PC with thinner TiO_2 layer.

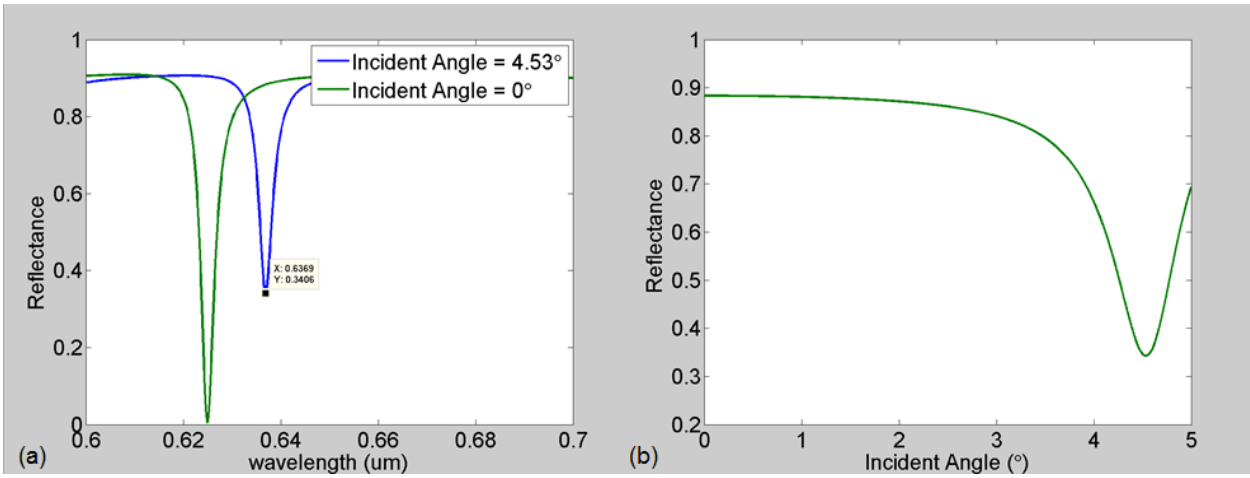

Figure 24 Far-field reflection simulations. (a) Far-field reflection spectra at normal incidence and θ = 4.53° incidence. (b) Angle spectrum at 637 nm excitation.

Table 3 Calculated enhancement factors for mirror-underneath PC with thinner TiO_2 layer at different excitation angle.

	Maximum enhancement factor	Average enhancement factor
0° Incidence	4.32	0
4.53° Incidence	86	26.24

From the tolerance analysis we learn that it is important to have precise control over TiO_2 thickness as well as incident angle.

3.4.3 Fabrication

From previous simulation and analysis, we finalize the mirror-underneath PC for fabrication. The mirror-underneath PC device is built on a silicon substrate (thickness = 2mm) with a titanium layer (thickness = 50nm), an aluminum layer (thickness = 100nm), patterned silicon dioxide layer (λ= 360 nm, duty cycle = 33%, cavity length = 205nm, grating height = 80nm) and a titanium dioxide layer (thickness = 119nm) on

top. The mirror-underneath PC structure is designed such that at normal-incidence excitation for TM polarization, resonance occurs at a wavelength of 632nm. We intentionally fabricate this device to resonate at shorter wavelength than excitation wavelength (637 nm) because absorption of the functionalization layer and protein/dye layer on the mirror-underneath PC surface will shift the resonant wavelength by a few nanometers. A commercial silicon foundry (Novati Technologies, Inc.) produces the mirror-underneath PC devices on 8-inch-diameter silicon wafers. Layers of titanium and aluminum are sputtered on the silicon. Then low-refractive index silicon dioxide (n=1.54) is grown by plasma-enhanced tetraethylorthosilicate (PETOS) because of its excellent step coverage. The periodic PC grating structure was defined by deep-UV photolithography and reactive ion etching. High-refractive-index titanium oxide film was deposited by reactive sputtering by a second commercial service that can provide uniform and reproducible dielectric thin films on 8-inch-diameter wafers (Intlvac Technologies). Figure 25 shows schematic, photo and SEM pictures of fabricated chips.

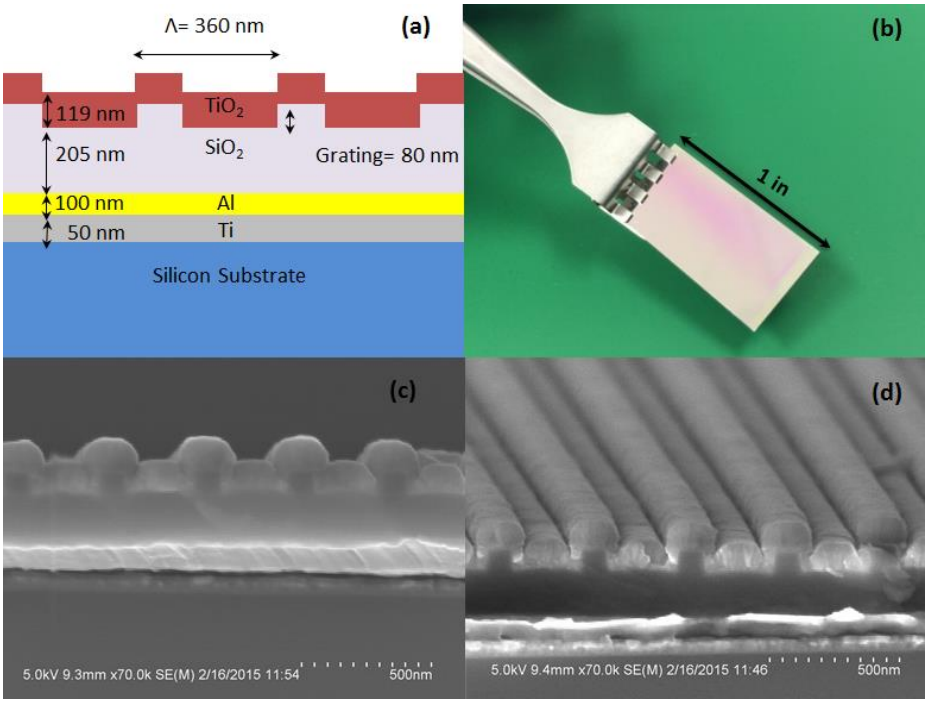

Figure 25 (a) Photo of a fabricated mirror-underneath PC (1 in × 0.5 in). (b) SEM picture (side-view). (c) SEM (cross-sectional view) fabricated mirror-underneath PC showing 1D grating in SiO_2 coated with TiO_2, SiO_2 cavity, aluminum layer and titanium layer on a silicon substrate.

3.4.4 Device characterization

We study the far-field spectrum and angle dependence of the mirror-underneath PC using the setup built by Chaudhery [19] shown in Figure 26. The setup consists of a tungsten halogen lamp (white light source) which couples to an optical fiber (Ocean Optics) with a 50 µm core. The output is collimated using an achromatic lens and polarized using a linear polarizer (Thorlabs Inc.). The detector height is lower than that of the incident beam and is coupled to another 50 µm core fiber. This setup enables the user to measure reflections at angle incidence θ.

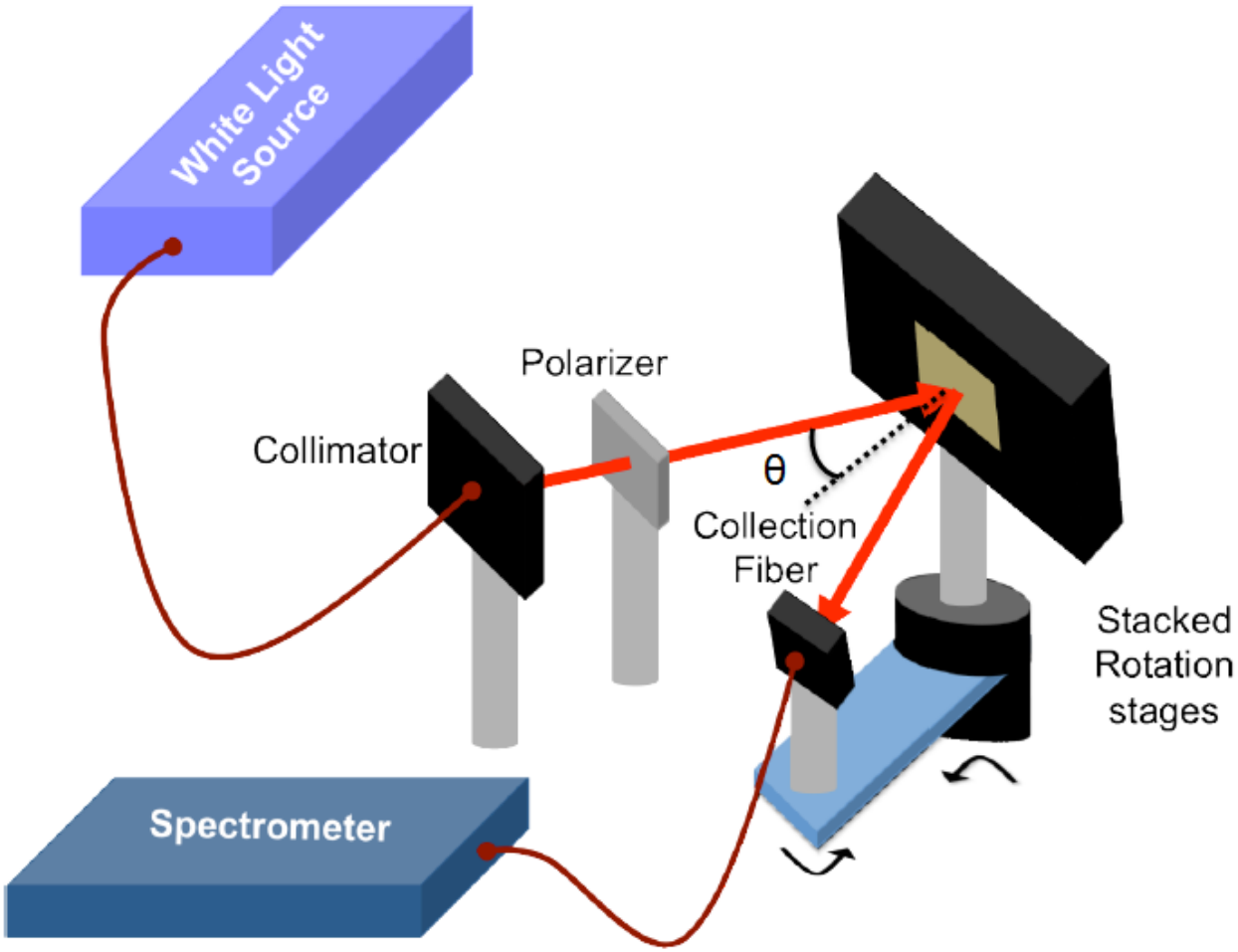

Figure 26 Schematic diagram of the reflection setup used for capturing reflected wavelength spectra [19].

Figure 27 (a) shows the far-field reflection spectra for the mirror-underneath PC with TM excitation. The black curve shows the measured reflection spectrum at normal incidence, showing a reflection dip located at 632 nm FWHM of ~3nm. And the red curve shows the measured reflection spectrum at θ = 1° excitation, showing a reflection dip located at 637 nm FWHM of ~3nm. The reflection dip location and intensity change rate are 5 nm/° and 20%/°, which are slightly larger than the predicted slope shown in Figure 23. Angle spectrum of 637 nm excitation is the blue curve in Figure 27 (b), showing a reflection dip at θ = 1° with FWHM of 0.77°. The band diagram is also obtained by the setup and is shown in Figure 28.

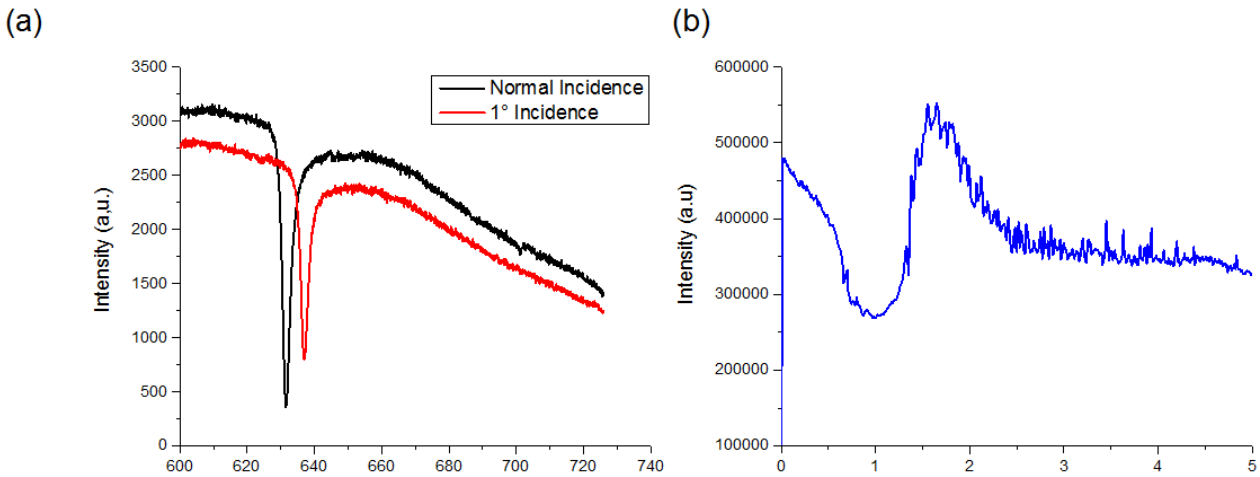

Figure 27 (a) Measured far-field reflection spectra. (b) Measured far-field angle spectrum with 637nm excitation.

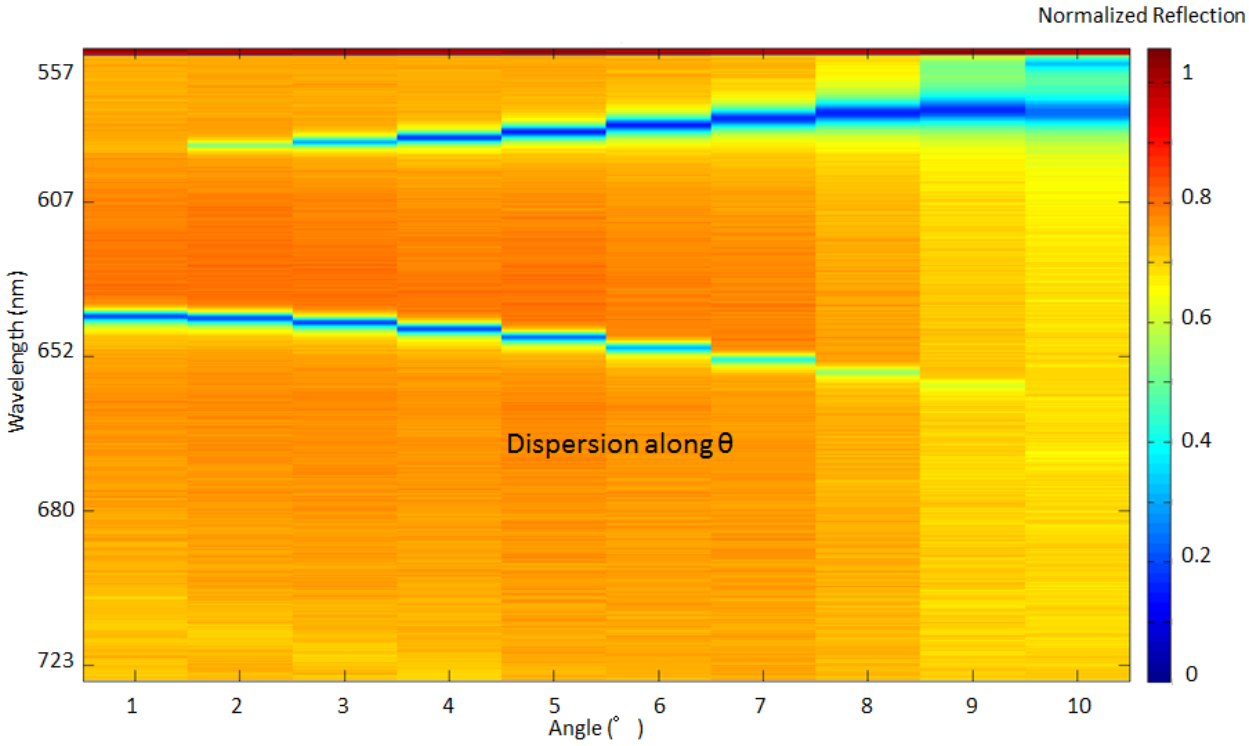

Figure 28 Measured band diagram for fabricated PC.

3.4.5 Coupled-cavity enhanced fluorescence

To demonstrate the enhancement of output signals from mirror-underneath PCs, ordinary PCs and glass slides, a simple detection experiment using fluorescent dye LD-700 (Exciton, Inc.) with peak absorption wavelength of 647 nm and a peak emission wavelength of 673 nm was conducted. Sample preparation process for each 0.5 inch by 1 inch ordinary PC, mirror-underneath PC and glass slide is as follows:

1. Sonicate each chip in acetone, isopropyl alcohol, and deionized water for 2 minutes to remove possible organic contaminations.
2. Dilute SU8 2000.5 with SU8 thinner (Microchem Corporation) at a volume ration of 1:12.
3. Dissolve LD-700 dye powder in methanol at 538 ng/ml, and then mix with diluted SU8 solution at a volume ratio of 1:2.
4. Spin coat the LD-700 doped SU8 onto the chips surfaces at 5000 rpm for 30 sec and then air dry.

The dye/polymer coated chips are tested using the PCEF benchtop line scanner shown in Figure 29. The illumination source of this system consists of a solid-state laser (AlGaAs) at 637 nm which is coupled to a sets of optical instruments. The resulting laser beam on PC is a TM polarized focused 6µm × 1mm line. The PCs are placed on a 2D-motorized stage which is translated perpendicular to the laser line for a fast scan. The emitted signal is collected by a CCD camera (Hamamatsu 9100C). A bandpass fluorescence filter can be inserted to block the excitation laser beam.

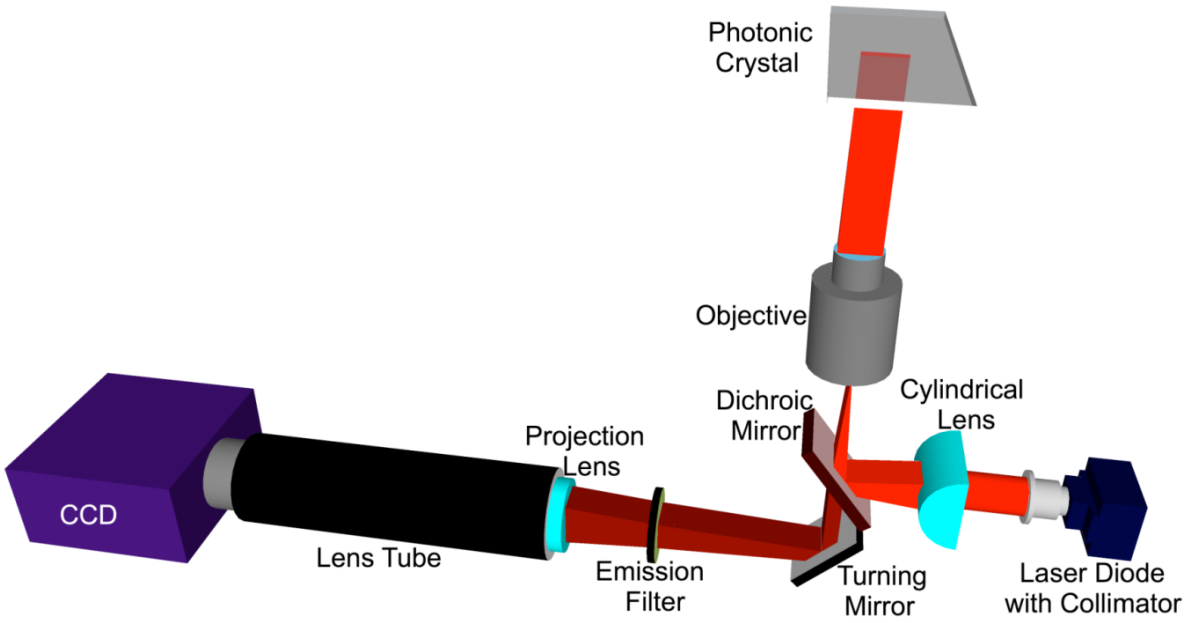

Figure 29 Schematic of the objective-coupled, line scanning instrument used to acquire fluorescence data at the precise PC resonant angle. Equipped with a solid-state laser diode, this instrument illuminates the PC with a beam of light that is focused in one plane for higher illumination density but collimated in the other plane for optimally coupling the incident light to the PC [19].

Figure 30 shows the captured fluorescent images of three chips and the intensity plot of the LD-700 fluorescence signals from the section of the chips illuminated with a single vertical line from the laser at normal incidence. From the intensity plots, we observed that increase in the intensity from the mirror-underneath PC chip was 15x greater than that from the silicon chip, and 3x greater than the ordinary PC.

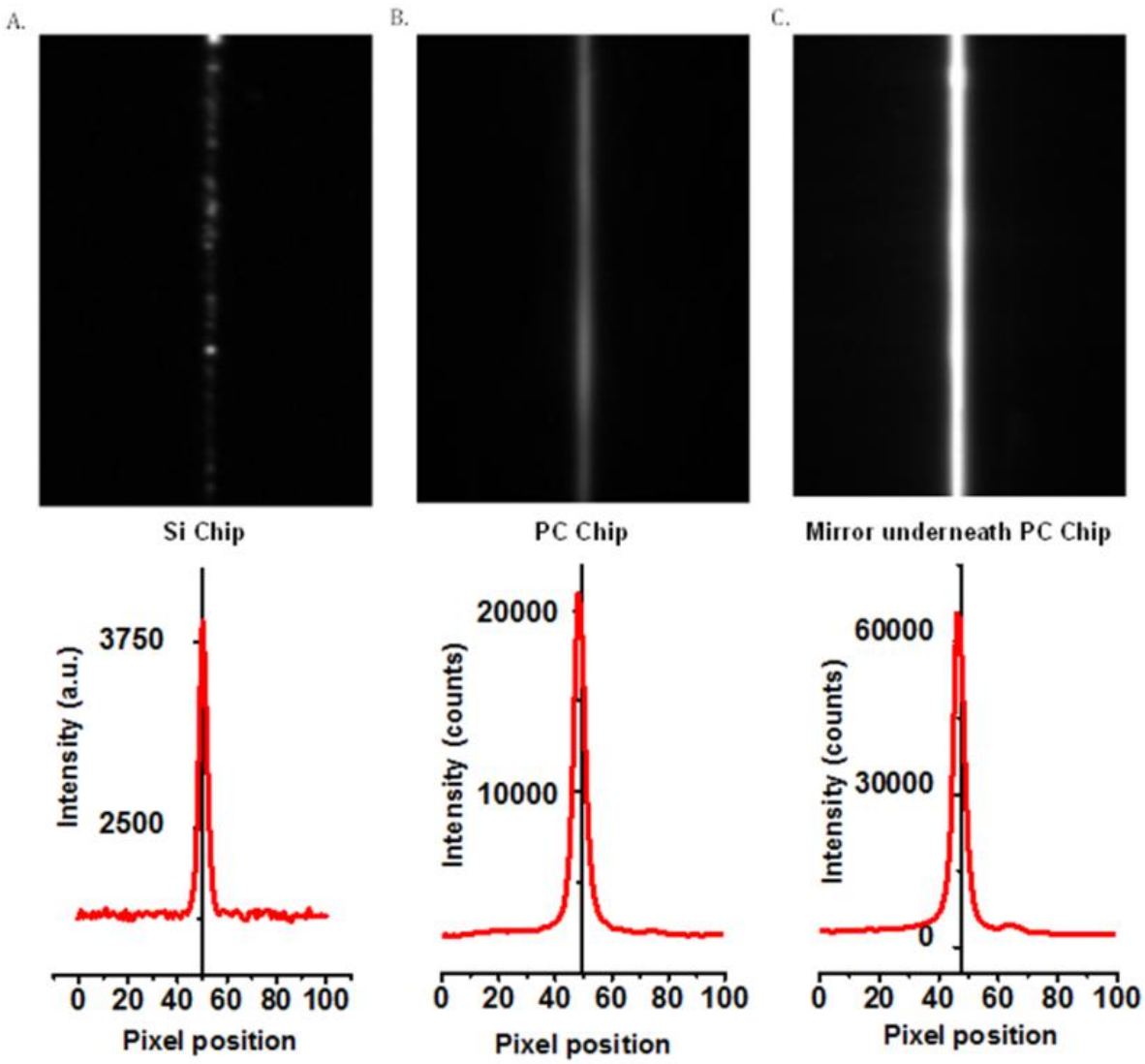

Figure 30 Intensity plots for (a) silicon chip, (b) PC chip, and (c) mirror-underneath PC chip, showing that mirror-underneath PC chip provides the highest enhancement of fluorescence signal. [Photo curtesy of Weili Chen]

3.4.6 Detection of dye labeled protein

In order to demonstrate the enhancement in the SNR and lowering of the limit of detection of the analytes on the mirror-underneath PC surface in the context of a multi-spot microarray assay, a detection experiment using a dye-labeled protein is performed. The sample preparation process for an ordinary PC and a mirror-underneath PC is as follows:

1. Sonicate each chip in acetone, isopropyl alcohol, and deionized water for 2 minutes to remove possible organic contaminations.
2. Perform O_2 plasma etching (Diener, Pico) on each chip for 3 min (100 W, 0.75 mTorr).
3. Adhere backside of each chip to the inside of glass container lid.
4. Pipette 200 µL of (3-Glycidoxypropyl) trimethoxysilane (GPTS, Sigma Aldrich, Saint Louis, MO) to glass container and put the lid on.
5. Put the glass container in a vacuum oven for an overnight incubation at temperature of 80 °C and a pressure of 30 Torr.
6. Detach chips from lid and sonicate in toluene, methanol, and DI water for 2 min each and dried under a stream of N_2.
7. Dissolve cyanine-5 (Cy5) conjugated streptavidin (GE Healthcare) in phosphate buffer saline (PBS) at a concentration of 10 µg/ml.
8. Print Cy-5 streptavidin solution using non-contact micro-dispensing system (Gesim Nano-Plotter 2.1) at room temperature in a humid chamber (relative humidity = 65%).
9. Incubate printed chips at room temperature in a humid chamber overnight.
10. Wash chips by gently dipping them in 0.01% (v/v) Tween-20 in PBS (PBST) for 20s, then rinse chips with deionized water three times and N_2 dry.

The resulting Cy-5 streptavidin spots have a diameter of ~120 µm with 200 µm center-to-center spacing. Figure 31 shows microscope images of printed spots on section of the mirror-underneath PC and the ordinary PC.

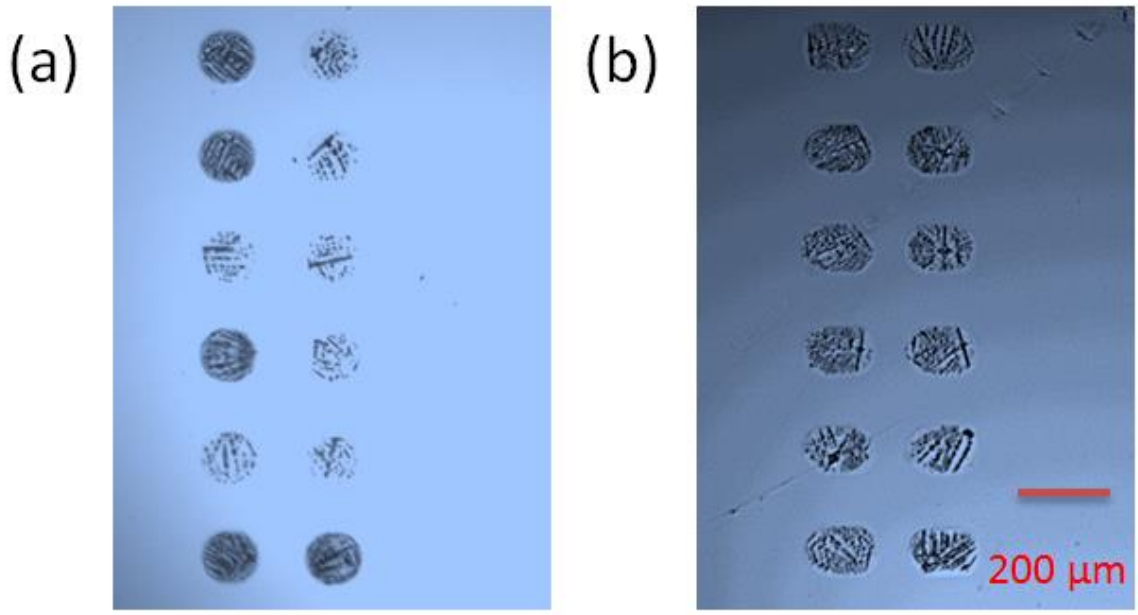

Figure 31 Microscope images of printed Cy-5 streptavidin spots on (a) mirror-underneath PC and (b) ordinary PC.

Fluorescent images of labeled protein spots were obtained by the benchtop line scanner using 40ms integration time and 70mA lasing power. The resonant angles of incidence were θ = 3.9 ° for the ordinary PC and θ = 0.4 ° for the mirror-underneath PC. The measured images were analyzed by image processing software (IMAGEJ). Figure 32 plots the intensity cross section through the Cy5 labeled protein spot on each device surface. The fluorescence intensity from Cy5 spots on mirror-underneath PC was higher than that from ordinary PC. From the intensity plot, the increase in the signal-to-noise ratio for the Cy5 spots on mirror-underneath PC was calculated as 5x that of the ordinary PC at on-resonance, and 10x that of ordinary PC at off-resonance. The noise here is defined as the standard deviation in the background intensity around the spot.

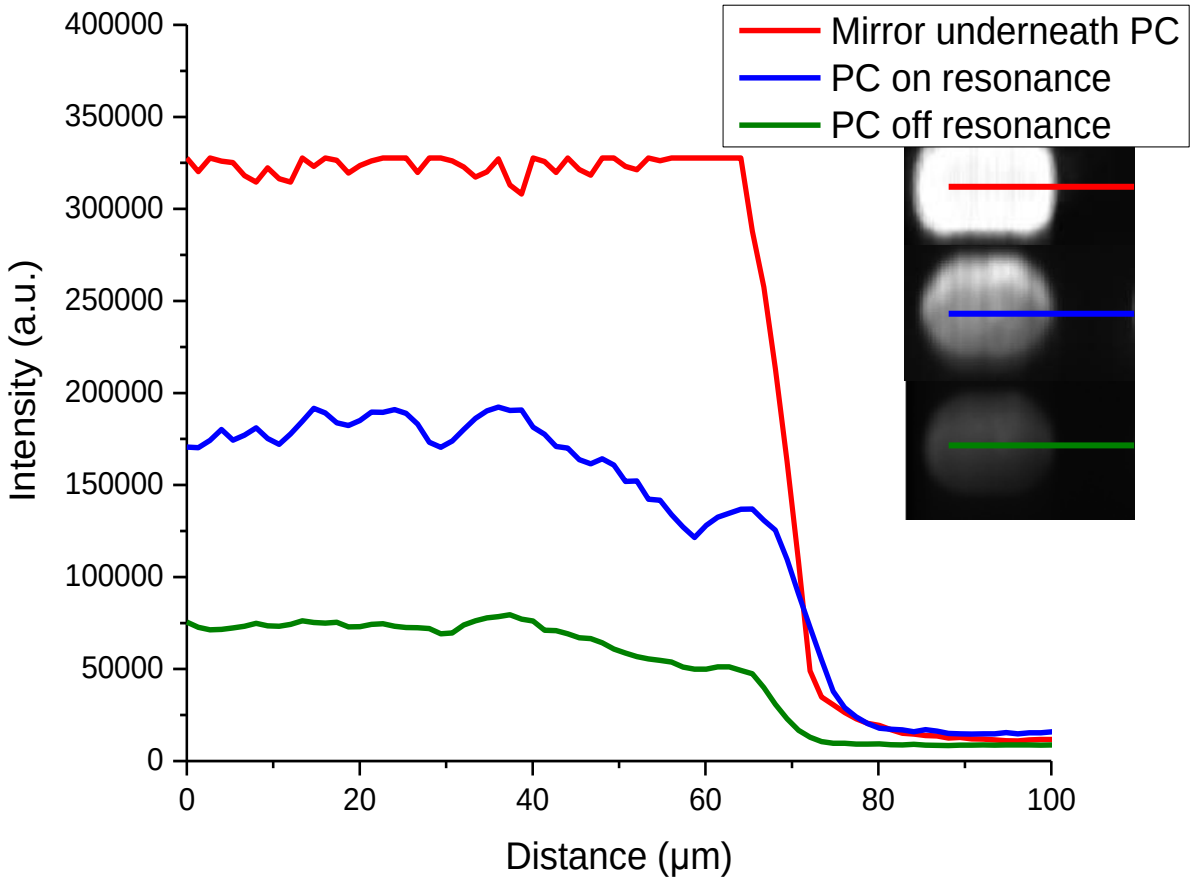

Figure 32 Intensity profile for Cy5 spots for the 3 devices (inset shown in same color scale): mirror-underneath, PC at on-resonance, and PC off-resonance

4. Future Work

4.1 Photobleaching on the mirror-underneath PC

It is reported that the photobleaching rate of dye molecules on the ordinary PC is accelerated by 30x compared to glass slide surface [20]. And since the mirror-underneath PC has greater ability to further increase surface electric field than ordinary PC, it will be insightful to learn how fast common fluorescent dyes used in fluorescent detections, like cyanine-5 and Alexa Fluor 647, photobleach on such surfaces and whether one can obtain substantial signal gain after long exposure to illumination at resonant condition.

4.2 Limit of detection

Because of the printer limitation, we cannot obtain uniform Cy5-labeled protein spots for all the concentrations, which prevents us from studying the limit of detection of the mirror-underneath PC. In the future, one should look into ways to get uniform dye-labeled protein spots by changing solvents or protein, and/or better understanding surface chemistry. Once uniform protein spot printing is achieved, one can measure fluorescent output from spots of varying concentration, and construct a standard curve that reveals the limit of detection.

4.3 Multiplexed detection of biomarkers and integration with microfluidics

Since the mirror-underneath PC provides stronger enhancement of evanescent field as well as SNR, it will be promising to use it as a surface for multiplexed and low concentration biomarker detection to break the detection limit. Also, by integrating the mirror-underneath PC with microfluidics, one will not

only save much valuable bio-sample and lower limit of detection, but also have better assay repeatability and less assay time.

5. Conclusion

In summary, this thesis briefly reviews the fluorescence phenomenon and PC enhanced fluorescence mechanisms. Then it demonstrates the work for further enhancing fluorescence output from the mirror-underneath PC. The mirror-underneath PC is built on silicon with a layer of aluminum mirror inserted between the silicon substrate and PC grating. The distance between PC grating and mirror layer is chosen to establish Fabry-Perot resonance. Simulations and experiments show that the coupling of PC resonance and Fabry-Perot resonance results in enhanced evanescent field. The new device is promising to improve SNR and sensitivity in surface-bound fluorescence assays used widely in disease diagnostics, DNA sequencing and drug research. There is still work to be done regarding the mirror-underneath PC as it is a relatively new device. For example, one can study the photobleaching rate on the mirror-underneath PC and think about approaches to integrate it with microfluidics for automated and rapid assays.

References

[1] J. Lakowicz, *Principles of fluorescence spectroscopy*. New York: Plenum Press, 1983.

[2] W. Deng, F. Xie, H. T. M. C. M. Baltar, and E. M. Goldys, “Metal-enhanced fluorescence in the life sciences: here, now and beyond,” *Phys. Chem. Chem. Phys*., vol. 15, no. 38, pp. 15695–15708, 2013.

[3] C. D. Geddes, J. R. Lakowicz, Metal-Enhanced Fluorescence, *Journal of Fluorescence*, vol. 12, no. 2, June 2002.

[4] P. P. Pompa, L. Martiradonna, A. Della Torre, F. Della Sala, L. Manna, M. De Vittorio, F. Calabi, R. Cingolani, and R. Rinaldi, “Metal-enhanced fluorescence of colloidal nanocrystals with nanoscale control,” *Nature nanotechnology,* vol .1, no 2, pp. 126-130, 2006.

[5] A. Kinkhabwala, Z. Yu, S. Fan, Y. Avlasevich, K. Müllen, and W. E. Moerner, “Large single-molecule fluorescence enhancements produced by a bowtie nanoantenna,” *Nat. Photonics*, vol. 3, no. 11, pp. 654–657, 2009.

[6] S. George, “Microarray-based biomarker detection using photonic crystal enhanced fluorescence and label-free imaging,” Ph.D. dissertation, University of Illinois at Urbana-Champaign, 2013.

[7] C. Ge, M. Lu, X. Jian, Y. Tan and B. Cunningham, “Large-area organic distributed feedback laser fabricated by nanoreplica molding and horizontal dipping,” *Opt. Express*, vol. 18, no. 12, p. 12980, 2010.

[8] J. Joannopoulos, S. Johnson, J. Winn and R. Meade, *Photonic crystals*. Princeton, NJ: Princeton University Press, 2008.

[9] R. W. Woods, "On a remarkable case of uneven distribution of Light in a diffraction grating Spectrum," *Proc. Phys. Soc. London,* vol. 18, pp. 269, 1902.

[10] D. Maystre, "Theory of Wood's anomalies," in *Plasmonics*, S. Enoch and N. Bonod, Eds.: Berlin and Heidelberg: Springer, 2012.

[11] S. G. Johnson, S. H. Fan, P. R. Villeneuve, J. D. Joannopoulos, and L. A. Kolodziejski, "Guided modes in photonic crystal slabs," *Physical Review B,* vol. 60, pp. 5751-5758, Aug. 15, 1999.

[12] A. Sharon, D. Rosenblatt, and A. A. Friesem, "Resonant grating waveguide structures for visible and near-infrared radiation," *Journal of the Optical Society of America a-Optics Image Science and Vision*, vol. 14, pp. 2985-2993, Nov. 1997.

[13] A. Pokhriyal, "Evanescent field enhanced fluorescence on a photonic crystal surface," Ph.D. dissertation, University of Illinois at Urbana-Champaign, 2013.

[14] A. Debnath, S. Kumar, D. V. Udupa, and N. K. Sahoo, "Design of narrow band notch filter based on guided mode resonance effect in thin film layers," *AIP Conference Proceedings,* vol. 301, pp. 301–303, 2012.

[15] A. Pokhriyal, M. Lu, V. Chaudhery, C.-S. Huang, S. Schulz, and B. T. Cunningham, "Photonic crystal enhanced fluorescence using a quartz substrate to reduce limits of detection," *Opt. Express*, vol. 18, no. 24, pp. 24793–24808, 2010.

[16] N. Ganesh, I. D. Block, P. C. Mathias, W. Zhang, E. Chow, V. Malyarchuk, and B. T. Cunningham, "Leaky-mode assisted fluorescence extraction: application to fluorescence enhancement biosensors," *Opt. Express*, vol. 16, no. 26, pp. 21626-21640, 2008.

[17] G. G. See, L. Xu, M. S. Naughton, T. Tang, Y. Bonita, J. Joo, P. Trefonas, K. Deshpande, P. J. A. Kenis, R. G. Nuzzo, and B. T. Cunningham, "Region specific enhancement of quantum dot emission using interleaved two-dimensional photonic crystals," *Appl. Opt*, vol. 54, pp. 2302-2308, 2015.

[18] A. Pokhriyal, M. Lu, V. Chaudhery, S. George, and B. T. Cunningham, “Enhanced fluorescence emission using a photonic crystal coupled to an optical cavity,” *Appl. Phys. Lett*., vol. 102, no. 22, 2013.

[19] V. Chaudhery, "Next generation instrumentation for photonic crystal biosensors: A passage to early detection of cancer," Ph.D. dissertation, University of Illinois at Urbana-Champaign, Urbana, IL, 2012.

[20] V. Chaudhery, M. Lu, C. S. Huang, S. George, and B. T. Cunningham, “Photobleaching on photonic crystal enhanced fluorescence surfaces,” *J. Fluoresc*., vol. 21, no. 2, pp. 707–714, 2011.